Mon. Not. R. Astron. Soc. **341,** 405–422 (2003)

Discovery of a precessing jet nozzle in BL Lacertae

A. M. Stirling,[1⋆] T. V. Cawthorne,[1] J. A. Stevens,[2,3] S. G. Jorstad,[4] A. P. Marscher,[4] M. L. Lister,[5] J. L. Gómez,[6,7] P. S. Smith,[8] I. Agudo,[6] D. C. Gabuzda,[9] E. I. Robson[10] and W. K. Gear[11]

[1]*CFA, University of Central Lancashire, Preston PR1 2HE*
[2]*Astronomy Technology Centre, Royal Observatory, Blackford Hill, Edinburgh EH9 3HJ*
[3]*Mullard Space Science Laboratory, University College London, Holmbury St Mary, Surrey RH5 6NT*
[4]*Institute for Astrophysical Research, Boston University, 725 Commonwealth Avenue, MA 02215, USA*
[5]*National Radio Astronomy Observatory, 520 Edgemont Road, Charlottesville, VA 22903-2454, USA*
[6]*Instituto de Astrofísica de Andalucía (CSIC), Apartado 3004, Granada 18080, Spain*
[7]*Institut d'Estudis Espacials de Catalunya/CSIC, Edifici Nexus, c/ Gran Capità, 2-4, E-08034 Barcelona, Spain*
[8]*Steward Observatory, University of Arizona, 933 N. Cherry Ave, Tucson, AZ 85721, USA*
[9]*Joint Institute for VLBI in Europe, Postbus 2, 7990 AA Dwingeloo, the Netherlands*
[10]*Joint Astronomy Centre, 660 N. A'ohoku Place, Hilo, HI 96720, USA*
[11]*Department of Physics and Astronomy, Cardiff University, PO Box 913, Cardiff CF2 3YB*

Accepted 2003 January 16. Received 2003 January 16; in original form 2002 September 29

ABSTRACT

We present the results of a multiwavelength campaign during which BL Lac was observed at 17 regular epochs from 1998.23 to 2001.28. We used the Very Long Baseline Array (VLBA) in an observing mode sensitive to linear polarization at wavelength 7 mm with a resolution of the order of 0.2 mas. For the first time such observations were complemented by near-simultaneous polarization-sensitive James Clerk Maxwell Telescope (JCMT) observations at a wavelength close to 1 mm. Optical polarimetry was also obtained for the final year of observations. The VLBA images reveal a remarkable oscillating 'nozzle' structure with a period of $\sim$2 yr. The orientation of the nozzle tracks the polarization position angle measured at the JCMT, in which we detect a very similar period. We argue that these results require the same jet direction at the small scale probed by the 1-mm emission as at the larger scale probed by the 7-mm emission; there is no evidence to suggest wiggling of the jet between these scales. The picture that emerges is of a straight but precessing jet where the components form a straight line near the core, but form an apparently curved locus at larger separations where components were ejected in different directions. Two further lines of evidence support this view. First, tracing the evolution of bright components showed straight paths and ejection angles consistent with the nozzle direction at the ejection time. Secondly, a simple model of a precessing nozzle was used to predict the inner jet structure. At most epochs the agreement between the model and data was good. On angular scales >2 mas from the core a transition occurs and most components bend to follow the usual southeasterly direction on deca-milliarcsecond scales. This precession is clearly analogous to that found in the galactic jet source SS 433 albeit with a higher jet speed and a smaller precession cone opening angle. The precession observed in SS 433 is believed to be caused by the interaction of a companion star with the accretion disc around the compact object. This suggests the possibility that the black hole from which the jet from BL Lac emerges is part of a binary system.

Key words: polarization – BL Lacertae objects: general – BL Lacertae objects: individual: BL Lac – radio continuum: galaxies.

⋆E-mail: amstirling@uclan.ac.uk

1 INTRODUCTION

BL Lacertae and related active galactic nuclei (AGN) sources represent a subclass of extragalactic radio emitters showing weak or no emission lines. It seems probable that emission lines in these 'BL Lac objects' are intrinsically weak rather than swamped by a synchrotron continuum extending up to optical and sometimes X-ray wavelengths (Padovani 1992). Broad Hα has been observed in BL Lac (Vermeulen et al. 1995), although the mass of ionized gas required is probably still rather small, of the order of a few $M_\odot$ (Corbett et al. 1996). This may suggest a weaker ionizing flux or less cool gas than seen in quasars, rather than none at all. The source of any synchrotron continuum emission is believed to be the bipolar jets ejected perpendicular to the accretion environment. These jets and their magnetic field orientations can be imaged on parsec scales or less using full-polarization very long baseline interferometry (VLBP).

The synchrotron mechanism produces highly linearly polarized emission (up to 70 per cent). For optically thin emission the polarized electric field is perpendicular to the projection of the source magnetic field on to the plane of the sky. Magnetized regions of thermal gas within and outside the emitting volume can rotate the polarization vectors (the degree of Faraday rotation varies as λ^2 for a homogeneous foreground screen). The magnetic field structure within a convolving beam or Faraday depolarization can reduce the percentage of linear polarization (e.g. Burn 1966).

Polarization observations of BL Lac objects show a strong trend for magnetic fields transverse to the local jet direction (Gabuzda & Cawthorne 2000; Lister 2001). This is usually explained as the result of compression of a largely tangled magnetic field by shock waves in the jet (Hughes, Aller & Aller 1989). There was a significant rotation measure (RM) in the Very Long Baseline Array (VLBA) radio core of BL Lac, -434 rad m^{-2} in 1997 April, observed between 6 cm and 13 mm. This is equivalent to an electron column density of $1.3 \times 10^{24}/B_{||}$ m^{-2}, with the line-of-sight magnetic field $B_{||}$ in nT (Reynolds, Cawthorne & Gabuzda 2001). Higher-frequency VLBP observations at 20, 13 and 7 mm detect a rather higher and variable RM in the radio core, up to 7500 rad m^{-2} (Mutel & Denn 2000). Clearly, some thermal gas is present between BL Lac and the observer. These derived radio core RMs for BL Lac are similar to those found in several quasars but higher than 3C345, for example (Taylor 1998, 2000).

In this paper we present images of the 17 observations of BL Lac, results from our millimetre wavelength monitoring programme. 15 sources were monitored in full polarization at 7 mm with the VLBA with additional monitoring at submillimetre wavelengths from the James Clerk Maxwell Telescope (JCMT) and optical wavelengths (Marscher et al. 1999; Jorstad et al. in preparation). The steep spectral index of the jets from AGN in the optically thin regime means we can only detect such sources out to a few mas from the core with the VLBA at 7 mm. The reduced source opacity and higher resolution at 7 mm, compared with previous mostly lower-frequency observations (Tateyama et al. 1998; Denn, Mutel & Marscher 2000), allowed observations of the radio core in more detail. The addition of the shorter wavelengths from the JCMT (0.85, 1.1 and 1.35 mm) and optical from the Steward Observatory 60-in telescope allowed investigation of the emission regions in radio, submillimetre and optical bands.

2 OBSERVATIONS AND DATA REDUCTION

2.1 VLBA data

Our 17 VLBA observations were taken at 6.94 mm (43.21 GHz), typically using all 10 antennas of the VLBA. The observing dates and telescopes present can be found in Table 1. The data were recorded in eight baseband (IF) channels of 8-MHz bandwidth. Both right- and left-hand polarizations were recorded with 1-bit sampling, giving an overall bandwidth of 32 MHz. The data were correlated using the VLBA correlator at Socorro, New Mexico. 12 scans of 6-min duration were taken on BL Lac at each epoch. Six epochs of supplementary data from a related project using BL Lac as a calibrator were also obtained at: 6.94 mm (B0); 6.94 and 13.49 mm (B1 and B2); and 6.94, 13.49 and 19.53 mm (B3, B4 and B5). Calibration was performed using the NRAO AIPS package (e.g. Fomalont 1981) in the standard way for VLBP (Roberts, Wardle & Brown 1994; Leppanen, Zensus & Diamond 1995). An opacity correction was made using unpublished flux densities of our target sources at similar epochs to derive the appropriate zenith opacities. These data were taken from Metsähovi quasi-stellar object monitoring at wavelengths 13 and 8 mm and provided by H. Teräsranta. The absolute electric vector position-angle (EVPA) rotations were derived using near simultaneous Very Large Array (VLA) observations for B0–B2 and by comparison of several sources with slowly varying EVPA values for epochs 1–17. For epochs B3–B5 the absolute EVPA calibration was performed by aligning an optically thin and polarized feature in the extended jet with the equivalent feature in the nearest correctly calibrated 7-mm data set. Detailed calibration information can be found in Jorstad et al. (in preparation).

Table 1. The observing dates for the BL Lac images presented in this paper. Supplementary data are marked B* for two observing wavelengths (7 and 13 mm) and B** for three observing wavelengths (7, 13 and 20 mm).

Epoch	Date	Equivalent date	Telescopes
1	1998 March 25	1998.23	All
2	1998 May 31	1998.41	All
3	1998 July 31	1998.58	All
4	1998 October 05	1998.76	All
5	1998 December 10	1998.94	All
6	1999 February 13	1999.12	All
7	1999 April 29	1999.32	Not NL
8	1999 July 17	1999.55	All
9	1999 October 06	1999.76	All
10	1999 December 05	1999.93	Not SC
11	2000 January 24	2000.07	All
12	2000 April 05	2000.26	All
13	2000 July 17	2000.54	All
14	2000 October 01	2000.75	Not BR
15	2000 December 11	2000.95	Not LA
16	2001 January 28	2001.08	Not LA, KP
17	2001 April 14	2001.28	All
B0	1997 July 30	1997.58	All
B1*	1999 January 10	1999.03	All
B2*	1999 February 10	1999.11	All
B3**	2000 June 29	2000.49	All
B4**	2000 November 03	2000.84	All
B5**	2001 March 23	2001.22	All

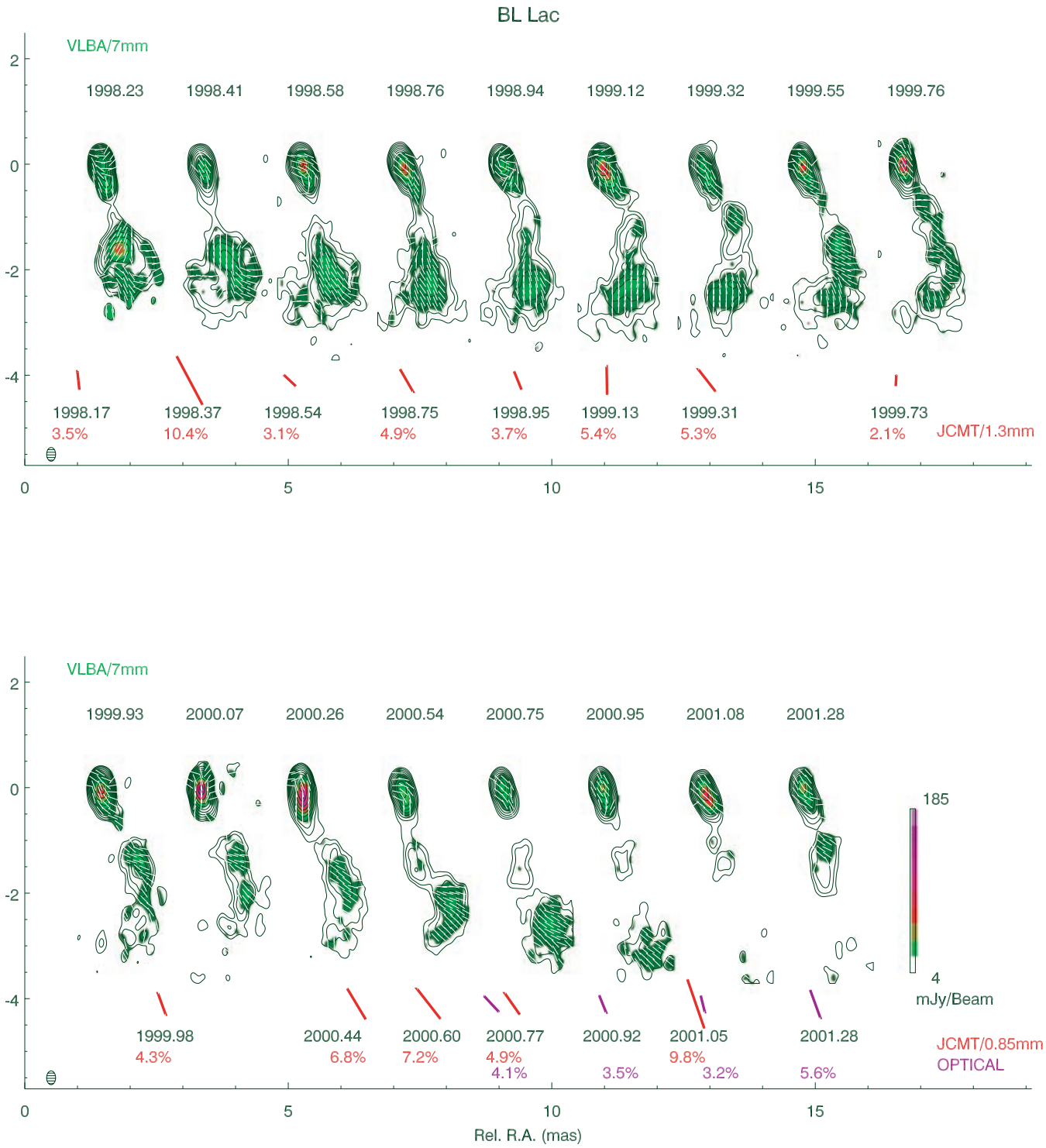

Figure 1. A montage of all 17 uniformly weighted VLBA epochs. The contours represent the total intensity, the colours represent linearly polarized intensity and the superimposed white sticks (of constant length) represent the EVPA. Plotted below these images are vectors indicating fractional linearly polarized emission $m = P/I$ (stick length) and EVPA (stick direction) at mm/submm (JCMT) and optical wavelengths.

After initial reduction the data were edited, self-calibrated and then imaged in Stokes *I*, *Q* and *U* using a combination of AIPS and DIFMAP (Pearson et al. 1994). The uniformly weighted images are convolved with the average restoring beam of 0.26×0.17 mas^2 with a position angle of 0°. The montage of final images is presented in Fig. 1. The contouring represents Stokes *I*, in factors of 2 from 0.00125 × the montage peak brightness, 3.86 Jy beam^{-1}. The colours represent polarized brightness, *P*, derived from $(Q^2 + U^2)^{1/2}$ and cut-off at 4 mJy beam^{-1}. The peak polarized brightness of 185 mJy beam^{-1} occurs at epoch 2000.07. The measured

electric vector position angle (EVPA) sticks are superimposed in white. We estimate typical errors of 20 per cent in absolute flux density calibration and 8° in EVPA.

2.2 JCMT data

Observations at 1.35 and 0.85 mm were performed at the James Clerk Maxwell Telescope using SCUBA (Holland et al. 1999) and its polarimeter (Greaves et al. 2003). The first eight epochs were observed using the 1.35-mm pixel because the sources are almost always brighter, the atmospheric opacity is lower and the sky is more stable than at 0.85 mm. However, failure of the SCUBA filter drum forced a switch to the full array operating at 0.85 mm. For these observations we placed the source in the central pixel and used the rest of the array to remove the sky noise that is correlated across the 2.3-arcmin field of view of SCUBA. It has been shown that the polarization properties of blazars are very similar at millimetre and submillimetre wavelengths (Nartallo et al. 1998) so the change in wavelength should not affect our analysis. Six archive epochs were obtained from Nartallo et al. (1998).

The SCUBA polarimeter consists of a rotating quartz half-waveplate and a fixed analyser that absorbs one plane of polarization. During an observation, the waveplate is stepped through 16 positions, and photometry data are taken at each position. One rotation takes approximately 6 min to complete, and the procedure results in a sinusoidally modulated signal from which the Stokes parameters can be extracted. A typical observation consists of 5–10 complete rotations of the waveplate. Flux calibration can be achieved in the standard manner with observations of the planets or JCMT secondary calibrators. The instrumental polarization ($\sim$1 per cent) was measured on each run by making observations of a compact planet, usually Uranus, which is assumed to be unpolarized at millimetre/submillimetre wavelengths.

Initial stages of the data reduction (nod compensation, flat-field, extinction correction and sky noise removal, if appropriate) were performed with the standard SCUBA data reduction package, SURF. Subsequent analysis was undertaken with the SIT polarimetry reduction software. Stokes parameters were extracted by fitting sinusoids to the data, either half-cycle (eight points) resulting in two estimates, or full-cycle (16 points), yielding only one estimate but generally giving better results with noisy data. Spurious measurements were removed by performing a Kolmogorov–Smirnov test on the collated data. The polarization and position angle, corrected for instrumental polarization and parallactic angle, were then calculated using averaged Stokes parameters.

These data are presented in Table 2. Total intensity photometry data from the JCMT at 0.85 mm were obtained from archival pointing experiments (Robson, Stevens & Jenness 2001) and are displayed (along with epochs 9–13 at 0.85 mm given in Table 2) in Fig. 2. The source shows dramatic flaring behaviour over the period of our 7-mm VLBA monitoring.

2.3 Optical data

Six epochs of optical photopolarimetric data were obtained during 2000 and 2001. All but the final observation were made using the Steward Observatory 60-in telescope located on Mt Lemmon, Arizona, and the 'Two-Holer' polarimeter (Moore, Schmidt & West 1987). The same instrument was used at the Steward Observatory Kuiper 61-in telescope on Mt Bigelow, Arizona, to obtain polarimetry and photometry of BL Lac in 2001 April. The results are shown in Table 3. Polarization measurements were unfiltered, covering

Table 2. Integrated flux density and polarization monitoring from the JCMT at 1.35 mm (epoch numbers marked * at 0.85 mm). Percentage linear polarization $m = P/I$. Archive data (A1–A6) were obtained at 1.1 mm.

Epoch	Date	I (Jy)	m (per cent)	EVPA (deg)
1	1998.17	3.46 ± 0.35	3.5 ± 0.2	6 ± 2
2	1998.37	2.22 ± 0.22	10.4 ± 1.2	28 ± 3
3	1998.54	2.86 ± 0.29	3.1 ± 0.7	47 ± 6
4	1998.75	2.83 ± 0.17	4.9 ± 0.3	30 ± 2
5	1998.95	2.39 ± 0.24	3.7 ± 0.6	22 ± 4
6	1999.13	2.18 ± 0.22	5.4 ± 1.9	1 ± 9
7	1999.31	2.02 ± 0.20	5.3 ± 0.9	38 ± 4
8	1999.73	2.45 ± 0.25	2.1 ± 0.6	177 ± 10
9*	1999.98	4.22 ± 0.42	4.3 ± 0.7	20 ± 4
10*	2000.44	2.17 ± 0.22	6.8 ± 0.7	31 ± 5
11*	2000.60	1.35 ± 0.14	7.2 ± 2.2	38 ± 8
12*	2000.77	1.35 ± 0.14	4.9 ± 0.9	35 ± 5
13*	2001.05	2.62 ± 0.26	9.8 ± 1.4	19 ± 4
A1	1991.43	1.89 ± 0.22	8.1 ± 0.7	23 ± 2
A2	1992.02	1.06 ± 0.11	8.1 ± 1.2	168 ± 4
A3	1992.81	1.95 ± 0.16	10.2 ± 0.9	48 ± 2
A4	1993.15	2.11 ± 0.22	7.2 ± 1.3	20 ± 5
A5	1994.15	0.98 ± 0.04	11.8 ± 3.6	19 ± 8
A6	1995.59	2.60 ± 0.20	3.0 ± 0.7	17 ± 7

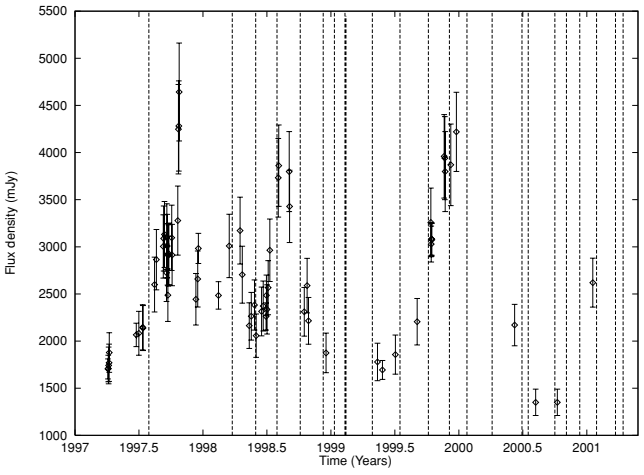

Figure 2. Total-intensity integrated flux density monitoring from the JCMT at 0.85 mm. Vertical lines indicate the VLBA epochs.

320–890 nm, with an effective wavelength of 650–700 nm, and employed a 0.94-mm circular aperture. For the $f/16$ 60-in telescope, the aperture corresponds to 8 arcsec on the sky (9.4 arcsec at the $f/13.5$ Kuiper telescope). On five of the six nights, differential V-band photometry of BL Lac using a 16.3-arcsec circular aperture at the 60-in telescope (19.2 arcsec at the Kuiper telescope) was obtained. Nearby field stars (Smith et al. 1985) were used to calibrate the photometry. Epoch 5 has no photometry because there was thin to moderate cirrus all night long. Since the moon was not in the sky, polarimetry was unaffected, but it was impossible to perform photometry using a single aperture and phototubes. The flux densities at 550 nm listed in Table 3 have been corrected for the estimated Galactic interstellar extinction in this sight line ($A_v = 1.091$; Schlegel, Finkbeiner & Davis 1998), and the fractional degree of linear polarization (m) has been corrected for Ricean bias (Wardle & Kronberg

Table 3. Integrated flux density and polarization monitoring at optical wavelengths. I represents extinction-corrected flux densities, observed apparent V magnitudes are also given. Percentage linear polarization $m = P/I$.

Epoch	Date	I (mJy)	V-band magnitude	m (per cent)	EVPA (deg)
1	2000.740	23.6 ± 0.5	14.06 ± 0.03	7.81 ± 0.17	36.8 ± 0.6
2	2000.742	30.3 ± 0.7	13.79 ± 0.03	0.84 ± 0.14	33.9 ± 4.7
3	2000.745	34.5 ± 1.3	13.65 ± 0.04	3.75 ± 0.15	57.2 ± 1.2
4	2000.915	27.4 ± 0.7	13.90 ± 0.03	3.47 ± 0.09	21.9 ± 0.8
5	2001.055			3.15 ± 0.21	14.3 ± 1.9
6	2001.290	16.8 ± 0.7	14.43 ± 0.04	5.55 ± 0.23	20.1 ± 1.2

1974). The 2000 September 27–29 polarization measurements have been averaged and plotted in Fig. 1.

3 RESULTS

3.1 7-mm VLBA data

Initial inspection of the 7-mm VLBA images shows that the total intensity structures are typical of previous high-frequency radio observations. The core is always the brightest feature, with a short collimated jet extending up to 1 mas from the core in position angle $\sim 210^\circ$. Here we see a region of minimum brightness where the jet bends, and a less collimated resolved jet traced up to a distance of 3–4 mas from the core. Component evolution in the jet shows typical apparent speeds of around 1.5 mas yr^{-1} with 1 mas $=$ $0.89\,h^{-1}$ pc for $z = 0.069$, $H_0 = 100\,h$ km s^{-1} Mpc^{-1} and $q_0 = 0.5$. The luminosity distance is therefore $210\,h^{-1}$ Mpc, giving apparent speeds $(\beta_{\rm app}) = 3.1\,h^{-1}\mu$, where μ is the proper motion in units of mas yr^{-1}.

The mean initial position angle of 194.0° (including supplementary data B0–B5) and the bend towards the southeast at 3–4 mas from the core are in agreement with the component evolution results of Denn et al. (2000) and Mutel et al. (1990). Of particular interest from these papers were the implied variable ejection directions of components from the radio core. Our data were model-fitted in order to examine this phenomenon in more detail.

3.1.1 Model fitting the total and polarized intensity

The self-calibrated I and P visibilities were model-fitted using the Brandeis VLBP package (Roberts, Gabuzda & Wardle 1987). The I and P visibilities were fitted separately to allow for differences in position of corresponding I and P components. An iterative method of selecting a starting model was employed. This involved fitting the core and jet with a few (usually three) very elongated Gaussian components that were each split in two when the fit had converged. This process continued until all components were circular, unless the associated χ^2 value increased. In this case the original elliptical component was reinstated. This procedure was chosen to give as much information on the local jet direction as possible in the initial 1 mas where the jet is not well resolved in the transverse direction (see Section 5.3).

A typical model fit in total intensity is shown in Fig. 3. Components fitted to the resolved jet (>1 mas from the core) can often be traced between epochs and therefore correspond to real enhanced brightness features. Analysis of the component trajectories is presented in Section 5. The flux densities of the inner jet components

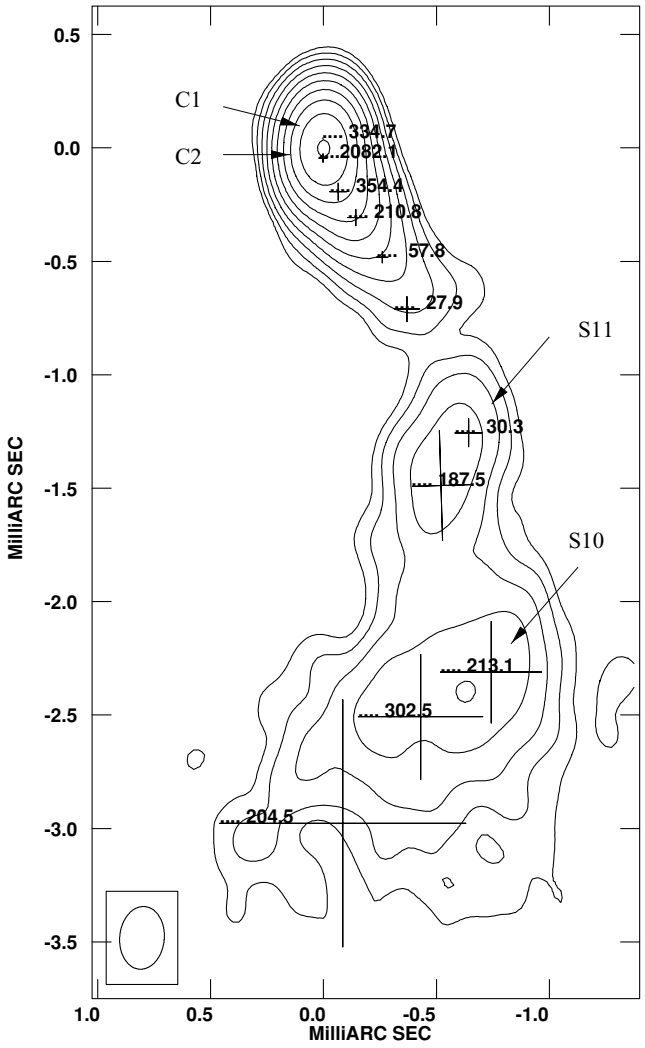

Figure 3. The results of the total intensity model fitting for the 1999 February 13 VLBA epoch. The numbers indicate the flux density of components in mJy while the crosses indicate the FWHM of each Gaussian component. The contours increment in factors of 2 from 0.003 Jy beam^{-1}, with an image peak of 1.617 Jy beam^{-1}.

(<1 mas) decrease monotonically with distance from the component at the phase centre in Fig. 3 to describe the ridge-line of a jet with a smoothly decaying brightness profile on these angular scales. The division of the brightness distribution into discrete components is a geometrical characterization that does not necessarily imply that these represent physically distinct regions of enhanced brightness. Two other trial models were also used to fit this inner jet structure: one circular Gaussian plus one elliptical Gaussian and two elliptical Gaussians. These were found to give comparable or significantly worse fits (χ^2 increased by as much as a factor of 2) to the overall structure, particularly when the core was bright with respect to the extended structure.

3.1.2 Radio core structural position angle

At all epochs the best total intensity model fit was obtained with a weaker component (which we denote by C1), ~0.1 mas north of the brightest component (which we denote by C2), with the brightest component located within 0.05 mas of the phase centre of the

Table 4. Results from fitting the base of the radio jet observed at 7 mm. Values of I, m and EVPA refer to component C2 only. Again, percentage linear polarization $m = P/I$. The structural position angle (SPA) is described in the text. C2/C1 is the ratio of the flux densities of C2 and C1. Separation refers to the projected angular separation of C1 and C2.

Epoch	Date	I (mJy)	m (per cent)	EVPA (deg)	SPA (deg)	C2/C1	Separation (mas)
B0	1997.58	1302 ± 261	2.46 ± 0.20	57.8 ± 9.4	185.4 ± 4.4	8.9 ± 0.6	0.09 ± 0.01
1	1998.23	2169 ± 434	1.58 ± 0.20	89.1 ± 19.7	201.1 ± 4.3	16.8 ± 0.7	0.08 ± 0.01
2	1998.41	1449 ± 290	1.93 ± 0.39	34.3 ± 10.0	200.5 ± 4.6	6.2 ± 0.3	0.08 ± 0.01
3	1998.58	3453 ± 691	2.37 ± 0.09	65.6 ± 8.1	214.6 ± 5.4	8.5 ± 0.7	0.08 ± 0.01
4	1998.76	1929 ± 386	3.44 ± 0.43	50.7 ± 8.1	208.0 ± 4.5	8.8 ± 0.5	0.08 ± 0.01
5	1998.94	1582 ± 316	2.10 ± 0.64	66.0 ± 8.4	194.4 ± 4.2	8.2 ± 0.2	0.08 ± 0.01
B1	1999.03	1098 ± 236	3.10 ± 4.11	34.6 ± 9.0	187.7 ± 6.3	1.6 ± 0.2	0.15 ± 0.01
B2	1999.11	1402 ± 281	2.00 ± 0.33	50.4 ± 9.4	187.8 ± 15.1	28.4 ± 14.9	0.14 ± 0.03
6	1999.12	2082 ± 417	4.12 ± 0.36	47.9 ± 8.7	181.7 ± 3.2	6.2 ± 0.1	0.09 ± 0.01
7	1999.32	1405 ± 281	1.71 ± 0.36	55.3 ± 8.5	191.6 ± 5.5	14.8 ± 2.1	0.06 ± 0.01
8	1999.55	2281 ± 456	3.52 ± 0.10	39.6 ± 8.7	179.6 ± 3.1	6.6 ± 0.1	0.09 ± 0.01
9	1999.76	2456 ± 492	5.59 ± 0.34	29.7 ± 8.2	174.5 ± 3.1	6.9 ± 0.5	0.10 ± 0.01
10	1999.93	3496 ± 700	2.01 ± 0.10	23.1 ± 8.1	191.2 ± 2.7	11.5 ± 0.5	0.12 ± 0.01
11	2000.07	2681 ± 537	6.42 ± 0.41	9.3 ± 9.2	183.2 ± 3.6	2.2 ± 0.1	0.08 ± 0.01
12	2000.26	1618 ± 324	6.17 ± 0.32	22.2 ± 8.1	191.7 ± 3.7	1.2 ± 0.1	0.09 ± 0.01
B3	2000.49	1130 ± 226	7.24 ± 0.22	35.9 ± 9.7	198.9 ± 6.4	6.6 ± 0.7	0.12 ± 0.01
13	2000.54	867 ± 174	2.12 ± 0.19	77.6 ± 12.5	201.8 ± 4.4	3.8 ± 0.1	0.08 ± 0.01
14	2000.75	709 ± 142	1.40 ± 0.28	52.1 ± 9.4	192.4 ± 3.6	4.2 ± 0.2	0.09 ± 0.01
B4	2000.84	882 ± 177	3.17 ± 1.11	36.6 ± 10.3	201.5 ± 7.1	3.1 ± 0.2	0.11 ± 0.01
15	2000.95	1373 ± 276	3.36 ± 0.37	39.1 ± 8.4	205.5 ± 3.2	4.2 ± 0.3	0.12 ± 0.01
16	2001.08	1021 ± 204	3.83 ± 0.28	34.8 ± 8.4	198.2 ± 5.1	3.2 ± 0.1	0.07 ± 0.01
B5	2001.22	745 ± 149	4.47 ± 0.86	49.1 ± 8.4	201.9 ± 8.5	4.0 ± 0.2	0.08 ± 0.01
17	2001.28	836 ± 167	5.12 ± 0.15	30.6 ± 8.1	187.9 ± 3.6	7.0 ± 0.4	0.09 ± 0.01

self-calibrated image. This may represent a partially opaque region in the transition from an optically thick to an optically thin jet (e.g. Königl 1981). The results from model fitting the base of the radio jet are given in Table 4, where I, m and EVPA refer to the component nearest the phase centre of the model fits to the I and P visibilities (C2). The structural position angle (SPA) refers to the angle between the line defined by the positions of the two most northern model-fitted components (C1 and C2) and north (measured east of north). C2/C1 is the ratio of the fitted total-intensity flux densities of C1 and C2. Approximate errors in component flux densities and positions were derived by stepping parameters in small increments and minimizing χ^2 at each step, performed using the Brandeis VLBP package (Roberts, Gabuzda & Wardle 1987). The derived errors in these positional data were typically 0.004 mas for C1 and 0.003 mas for the rather brighter C2. These values were adopted for all epochs except for the supplementary epochs B0–B5 where positional errors of up to 0.03 mas for C1 and 0.005 mas for C2 were found. The range of errors in component positions gave errors of 3°–15° in the SPA of the radio core.

A marginally significant linear correlation coefficient, r, was found between the beam angle and the SPA ($r = 0.5$ at 98 per cent confidence), however, we tested seven epochs by editing the uv coverage in order to skew the beam angle by up to ±50°. The change in measured SPA was found to be 0.06 × the change in the beam angle, giving a much smaller bias than the quoted errors in the SPA. We conclude that the correlation between the beam angle and SPA was almost entirely spurious.

The variations in the SPA of these two components closest to the active nucleus are shown in Fig. 4. An oscillation of this SPA covering ∼30° is clearly apparent from inspection of this figure (and indeed the sequence of images in Fig. 1). A very similar oscillation was also found by replacing C1 and C2 with a single elliptical Gaussian and measuring its major-axis position angle in the model-fitting process. Using the single elliptical Gaussian gave position angle errors that were comparable to or smaller than the errors derived using two circular Gaussian components (C1 and C2) as shown in Fig. 3.

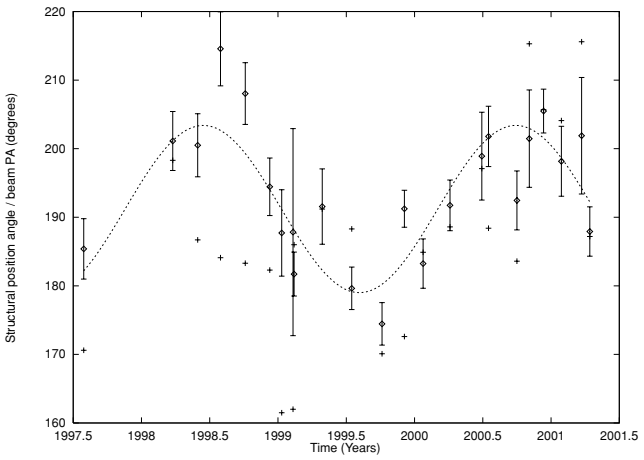

Figure 4. The SPA of the base of the jet as a function of time. The dotted line shows the best-fitting sinusoid to these VLBA data (including the supplementary data). The crosses show the beam position angle at each epoch.

The starlink package PERIOD was used to investigate the periodicity, utilizing a Lomb Scargle periodogram (Horne & Baliunas 1986), a cleaned Fourier transform (FT) and a χ^2 minimization. A χ^2 minimization for all four free parameters in a sine wave fit was performed giving a period of 2.29 ± 0.35 yr. The results of these period searching methods are given in Table 5. Approximate 1σ

Table 5. Table of period fitting results for these 7-mm SPA data. The phase zero corresponds to the time closest to the start of our observations that the position angle is equal to the offset (the mean PA in the sinusoidal fit). False alarm probability 1 (FAP1) is the probability that no periodic component at this frequency is present in the data. False alarm probability 2 (FAP2) is the probability that the period is not equal to the quoted value.

Method	Period (yr)	Min. error (yr)	FAP1	FAP2
Lomb Scargle	2.32	0.05	0.005 ± 0.005	0 ± 0.01
clean FT	2.27	0.05	0 ± 0.01	0 ± 0.01
Minimized χ^2	2.29	0.05	0 ± 0.01	0 ± 0.01
Best four-parameter fit	Period (yr)	Phase zero	Offset (deg)	Semi-amplitude (deg)
	2.29 ± 0.35	1997.88 ± 0.22	191.2 ± 5.5	12.2 ± 7.8

errors for the four-parameter fit were derived by normalizing the errors such that the reduced $\chi^2 = 1$ and then taking the uncertainties to be the range of a model parameter that introduces a total change of $\Delta\chi^2 = 1$ (e.g. Eikenberry et al. 2001). The final four-parameter fit had a reduced χ^2 (standard deviation) of 2.1 (5.7), while using the mean SPA of 194.0° gave a reduced χ^2 of 6.5 (9.9). It appears that the best-fitting sine wave is a good fit to these data (with $r = 0.82$ with >99.9 per cent confidence), although statistically significant residuals are present. Certainly it is a much improved fit over one using the model of a constant SPA.

3.1.3 EVPA measurements in the radio core

We have shown that these 7-mm total intensity data are broadly consistent with the position angle of the jet base sinusoidally oscillating on the plane of the sky. It was noted earlier that intrinsic core EVPAs in BL Lac objects tend to be aligned with the local jet direction (Gabuzda & Cawthorne 2000; Lister 2001). If this is true for BL Lac then we should see an agreement in the core EVPA as measured at 7 mm with the structural PA also measured at 7 mm. The core EVPA was taken as that measured for component C2, as C1 was almost always found to be unpolarized. The evolution of (EVPA−SPA) with time is shown in Fig. 5.

Interesting features of this plot are the tendency for a positive (EVPA > SPA) offset with a mean of 30°.9 and the generally smooth evolution with time. The near simultaneous measurements at 1999.11 and 1999.12 agree to better than 5°. However, between 2000.49 and 2000.54 we see a rapid variation of almost 40°, quickly returning to a more typical offset by 2000.84. There is a large deviation (68°) from good alignment at 1998.23, almost consistent with being perpendicular to the local jet direction within errors.

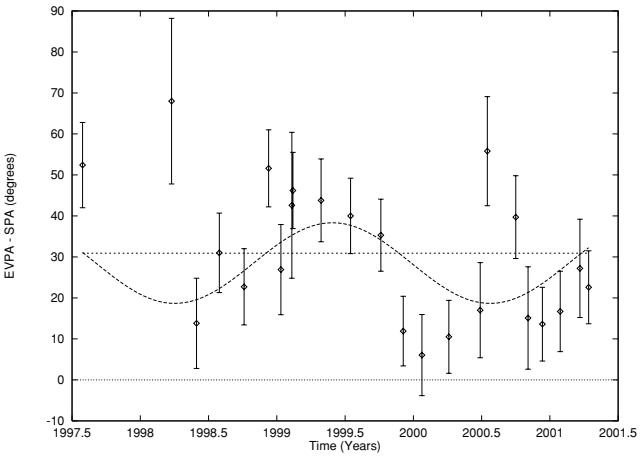

Figure 5. The offset between the EVPA and the structural position angle shown as a function of time. The dotted lines show the best sinusoidal fit to these VLBA data (including the supplementary data) and the mean value.

In order to investigate any correlation between EVPA misalignment and the oscillation described in the preceding section we performed the same period-searching methods as in the previous section. We found no unambiguous period detection from any of these methods. In Fig. 5 we also show a comparison of these (EVPA−SPA) data with the four-parameter sinusoidal fit that minimized the associated χ^2 value (with a period of 2.31 yr, a phase zero of 1998.73, an offset of 28°.5 and a semi-amplitude of 9°.8). The final four-parameter fit had a reduced χ^2 (standard deviation) of 2.3 (17.3) while using the mean (EVPA−SPA) of 30.9° gave a reduced χ^2 of 2.4 (17.1). We conclude that while these (EVPA−SPA) data vary considerably with time there is no statistically significant period detection.

3.2 JCMT linear polarization results

Although we are unable to resolve BL Lac with the single dish of the JCMT we can measure the integrated EVPA. The brightest polarized feature in the extended jet at 7 mm, with $m = 15$ per cent, was S10 at epoch 1998.23 (see Section 5). Assuming an optically thin synchrotron spectrum S10 contributed less than one-third of the integrated flux density in linear polarization at 1.35 mm. Other epochs would be less contaminated by emission from the extended jet at 1.35 mm, particularly after the change to 0.85 mm. We found large differences between the core EVPA at 7 mm and the integrated EVPA at 1.35 mm at some epochs (e.g. >45° at 1999.12/1999.13). We measured the polarized flux density in the extended 7-mm jet at epoch 1999.12, correcting for spectral index effects gave a contribution of 19 per cent to the integrated value at 1.35 mm. Even if the EVPAs in the extended jet were perpendicular to those in the core the difference between core and integrated EVPA would only be 11°. We also found a significant variation in EVPA with frequency at epoch 2001.05/2001.08 when almost no extended jet was seen at 7 mm. It appears then that a flat spectrum core dominates the polarized flux density at 1.35 mm. The differences in EVPA at 7 and 1.35 mm are not a result of the contaminating effect of extended jet emission at 1.35 mm. As the EVPAs of components in the extended jet are in rough alignment with the core direction the effect of extended emission on the integrated EVPA would be small, probably $\leqslant 5°$.

Fig. 6 shows the evolution of EVPA with time over the period of our JCMT monitoring and the archive data (A1–A6). Again there is a wide range (∼50°) in the observed electric field orientation. These EVPA data from the JCMT were used to perform the same period analysis as described in Section 3.1.2. Removing the furthest outlier (1999.31) improved the reduced χ^2 from 12.1 to 7.7. The

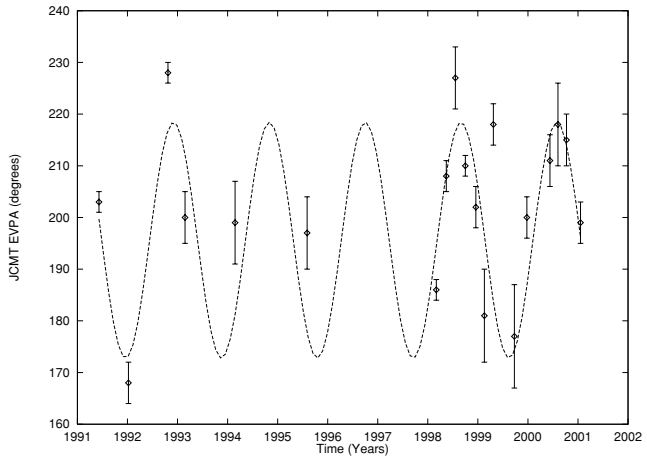

Figure 6. The integrated EVPA as measured by the JCMT shown as a function of time. The dotted line shows the best fit to these edited JCMT data.

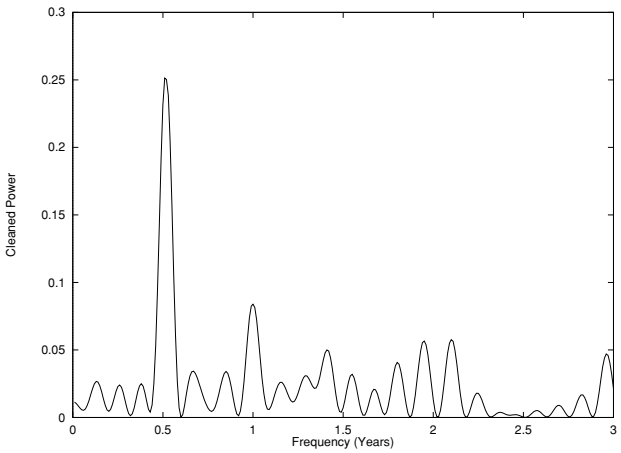

Figure 7. The cleaned power spectrum of these detrended JCMT integrated EVPA measurements without the 1999.31 data point.

results for the fit to these edited data are shown in Table 6. The final four-parameter fit had a reduced χ^2 (standard deviation) of 7.7 (10.2) while using the mean EVPA of 201.6° gave a reduced χ^2 of 22.0 (16.2). Here a sinusoidal model is again a reasonable characterization of these data (with $r = 0.70$ with >99.5 per cent confidence) and much better than that of a constant EVPA. However, we have one large deviation from the sinusoidal model and larger residuals than were observed for the SPA time series. The cleaned power spectrum of these edited and detrended EVPA data is shown in Fig. 7. A significant period detection is apparent and confirmed using the period search techniques within PERIOD (Table 6). We note that the JCMT total-intensity monitoring displays a deep minimum at the time of the discrepant EVPA measurement (1999.31) and the radio-core component C2 is weak in both total flux density and percentage polarization at the near-simultaneous epoch 1999.32.

3.3 Variable optical emission

There is a general correspondence between the optical EVPAs (Table 3) and those measured by the JCMT (Table 2), although there are few optical measurements as monitoring did not commence until late 2000. In addition, the optical data of 2000 September give an example of the flux density and polarization variations that BL Lac can exhibit. In a 2-day period the object brightened by nearly 50 per cent and became nearly unpolarized after $m \sim 8$ per cent on the previous night. Significant polarization variations on time-scales of an hour or less have been observed (Moore et al. 1982, 1987; Brindle et al. 1985). Despite the dramatic polarization and flux density variations that occur, the optical EVPA generally stays in the range of 0°–55°. Hagen-Thorn, Marchenko & Yakovleva (1985) summarize the optical polarization measurements of BL Lac from 1966 to 1982 and point out an average EVPA of ∼20° and that $m > 10$ per cent is observed only when the EVPA is within the preferred range (0°–55°). Excursions by the EVPA out of this range during this period were accompanied by $m < 10$ per cent.

Although the long-term optical EVPA trends for BL Lac and the data presented from 2000 and 2001 imply a connection with the submillimetre polarization and the VLBA polarization and structural PAs, its rapid variability make it difficult to determine a direct relationship between the optical emission region(s) and those producing the lower-frequency emission. Clearly, better optical coverage over a more extended period is needed to see whether the optical polarization generally tracks the submillimetre EVPA. Another approach would be to obtain simultaneous submillimetre and optical polarization measurements of a large number of sources to test whether the EVPAs in both frequency regimes are indeed related.

4 ANALYSIS OF THE CORE BEHAVIOUR

4.1 Correlated oscillations at 7 and 1 mm

We have detected an underlying oscillation in the structural position angle of the radio core as observed at 7 mm. The derived period of 2.29 ± 0.35 yr corresponds to over 1.5 cycles during the duration of our monitoring, 3.7 yr. Observations throughout a reasonable number of periods will be required to establish whether the behaviour is truly periodic.

The EVPA measurements from the JCMT also show a similar periodic oscillation, with period, phase, semi-amplitude and offset all consistent with those of the 7-mm SPA within approximate 1σ errors. The EVPA measurements at these submillimetre frequencies should be relatively unaffected by Faraday effects, and so provide a good estimate of the intrinsic magnetic field direction. The agreement between the four-parameter fits to the SPA and JCMT EVPA strongly support a transverse magnetic field in the early radio jet.

Table 6. Table of period fitting results for these EVPA data from the JCMT. FAP1 and FAP2 are as described in Table 5.

Method	Period (yr)	min. error (yr)	FAP1	FAP2
Lomb Scargle	1.92	0.04	0.03 ± 0.01	0 ± 0.01
clean FT	1.96	0.04	0.13 ± 0.02	0.01 ± 0.01
Minimized χ^2	1.92	0.04	0.15 ± 0.03	0 ± 0.01
Best four-parameter fit	Period (yr)	Phase zero	Offset (deg)	Semi-amplitude (deg)
	1.92 ± 0.08	1998.19 ± 0.16	195.5 ± 8.3	22.8 ± 11.9

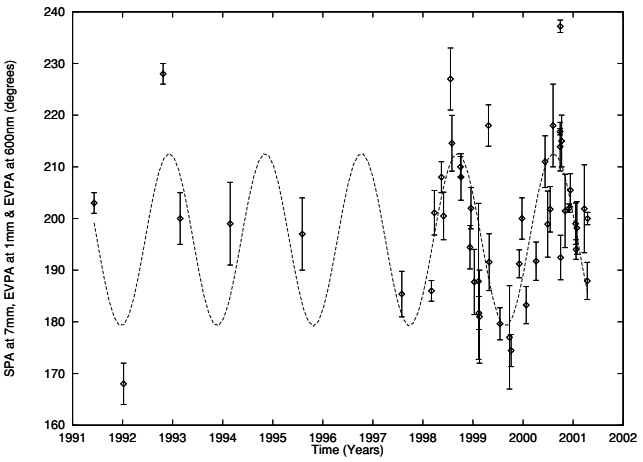

Figure 8. A comparison of the EVPAs from the JCMT observations, supplemented with archive data dating back to 1991, the 550 nm EVPAs and the SPA from the 7-mm VLBA data.

The need to edit the 1999.31 JCMT measurement indicates that more complex effects than a simple oscillation are also present. The SPA and JCMT/optical EVPA time series are plotted together in Fig. 8 with a best sine-wave fit to all 42 data points (excluding the optical data, for which a correlation has yet to be demonstrated). The fitted parameters gave a period of 1.92 yr, a phase zero of 1998.21, an offset of 195°.9 and a semi-amplitude of 16°.7 with a resultant reduced χ^2 of 7.4.

As a further check of any correlation between the 7-mm SPA and JCMT EVPA a cross-correlation test was performed. The 23 VLBA SPA measurements and the 13 near simultaneous JCMT EVPA measurements were each linearly interpolated and the cross-correlation performed for lags of -3 to 3 yr. The maximum cross-correlation coefficient was 0.67 when the VLBA SPA lagged the JCMT EVPA by 0.03 yr (with a FWHM of 0.50 yr). This is indicative of a positive linear correlation between these data sets with a time delay of magnitude less than or comparable to the mean sampling interval (0.19 yr). We find minimum cross-correlation coefficients of -0.47 and -0.35 (i.e. anticorrelation) at lags of ± 1.1 yr, consistent with noisy sinusoidal input signals of period $\sim$2.2 yr. Ideally, JCMT measurements with similar temporal resolution should be extended to cover several periods to verify the periodicity and the level of correlation with the SPA. Inspection of Fig. 1 suggests that the optical EVPA is in good agreement with the JCMT EVPA, although more coincident observations are needed to make any firm conclusions.

We note that our observation of a correlation between 0.85/1.3-mm EVPA and 7-mm SPA does not require that the emission regions are exactly co-spatial. Instead the jet must be relatively straight out to the radio core and the projected separation of the emission regions at 0.85/1.3 and 7 mm must be less than the apparent speed multiplied by a small fraction of the period.

4.2 Frequency dependence of the radio core EVPA

With good time coverage in only two observing frequencies from our primary data we utilized the multifrequency supplementary data to investigate the observed EVPA misalignment with respect to the SPA (see Section 3.1.3). Absolute calibration of the EVPA using the VLA at 7 mm was unavailable for epochs B3–B5. These data were model-fitted in the standard way using the Brandeis VLBP package. An attempt to calibrate the absolute EVPA at 7 mm correctly for data sets B3–B5 was made by aligning an optically thin and polarized feature in the extended jet with the equivalent feature in the correctly calibrated 7-mm data sets shown in Fig. 1. In all three cases the polarized feature selected could be found in the 13- and 20-mm model fits.

Table 7. EVPAs, fractional linear polarizations and total flux densities for component C2 at all frequencies derived from the supplementary epochs. An error of 5° is assumed for interpolated JCMT EVPA measurements.

Epoch	Wavelength (mm)	Core EVPA (deg)	m (per cent)	I (mJy)
B1	1.3	18.7 ± 5.0	–	–
B1	7	34.6 ± 11.8	3.10 ± 4.11	1098 ± 236
B1	13	80.6 ± 11.0	2.57 ± 0.23	1612 ± 323
B2	1.3	13.7 ± 5.0	–	–
B2	7	50.4 ± 13.1	2.00 ± 0.33	1402 ± 281
B2	13	91.4 ± 11.5	3.58 ± 0.17	1546 ± 309
B3	0.85	33.2 ± 5.0	–	–
B3	7	35.9 ± 13.5	7.24 ± 0.22	1130 ± 226
B3	13	67.9 ± 15.5	1.64 ± 0.37	1639 ± 328
B3	20	168.3 ± 9.0	3.34 ± 0.10	1594 ± 319
B4	0.85	29.3 ± 5.0	–	–
B4	7	36.6 ± 14.5	3.17 ± 1.11	882 ± 177
B4	13	92.6 ± 12.0	1.68 ± 3.44	1105 ± 221
B4	20	147.9 ± 9.9	1.58 ± 0.10	1082 ± 217
B5	0.85	8.4 ± 5.0	–	–
B5	7	49.1 ± 10.1	4.47 ± 0.86	745 ± 149
B5	13	115.0 ± 10.5	2.50 ± 0.26	848 ± 170
B5	20	137.3 ± 12.5	1.02 ± 0.13	889 ± 178

On angular scales greater than $\sim$1.5 mas from the core the jet RM is consistent with zero (Reynolds et al. 2001) and the Galactic RM is small (-108 rad m^{-2}). The 13- and 20-mm model fits were rotated so that the polarized feature used in the alignment process has an identical EVPA at 7, 13 and 20 mm for data sets B3–B5. This should result in a correctly calibrated core EVPA at all frequencies (except for the effect of the Galactic RM, which can be subtracted from the total derived RMs). The core EVPA at the appropriate JCMT frequency was calculated from the sine wave fit to the edited JCMT data set as shown in Fig. 6. The final values of EVPA at each frequency and epoch can be found in Table 7. The EVPA values for each epoch are plotted against wavelength squared (λ^2) in Fig. 9. Rotations of 180° are allowed as we do not measure the sense of the magnetic field line. For epochs B3 and B5 it was found that a much improved fit could be achieved by allowing the EVPA of the longest observing wavelength (20 mm) to rotate by 90°, as would be appropriate if the core is self-absorbed at this frequency. It is hard to justify this from the spectra of the core components that are very flat for all except B1. However, the excellent fit to a λ^2 dependence for B4 over a range of 110° argues against internal Faraday rotation where deviations from $\propto\lambda^2$ are found with rotations $>$45° for a uniform sphere and $>$90° for a uniform slab (Burn 1966). The results from this Faraday rotation analysis are given in Table 8. The derived RMs are probably caused by external Faraday rotation and are large and variable, 2000–10 000 rad m^{-2}. The derotated EVPAs for B1–B5 are compared with the SPA in Table 9 and show a better agreement with the SPA than the observed EVPAs at 7 mm.

The standard conical jet model (Königl 1981) is a fair approximation of the quiescent core. Here the observed core region moves further from the central engine as the observing wavelength increases. If we are observing the EVPA in different regions of the jet at each frequency then the intrinsic EVPA must be similar in

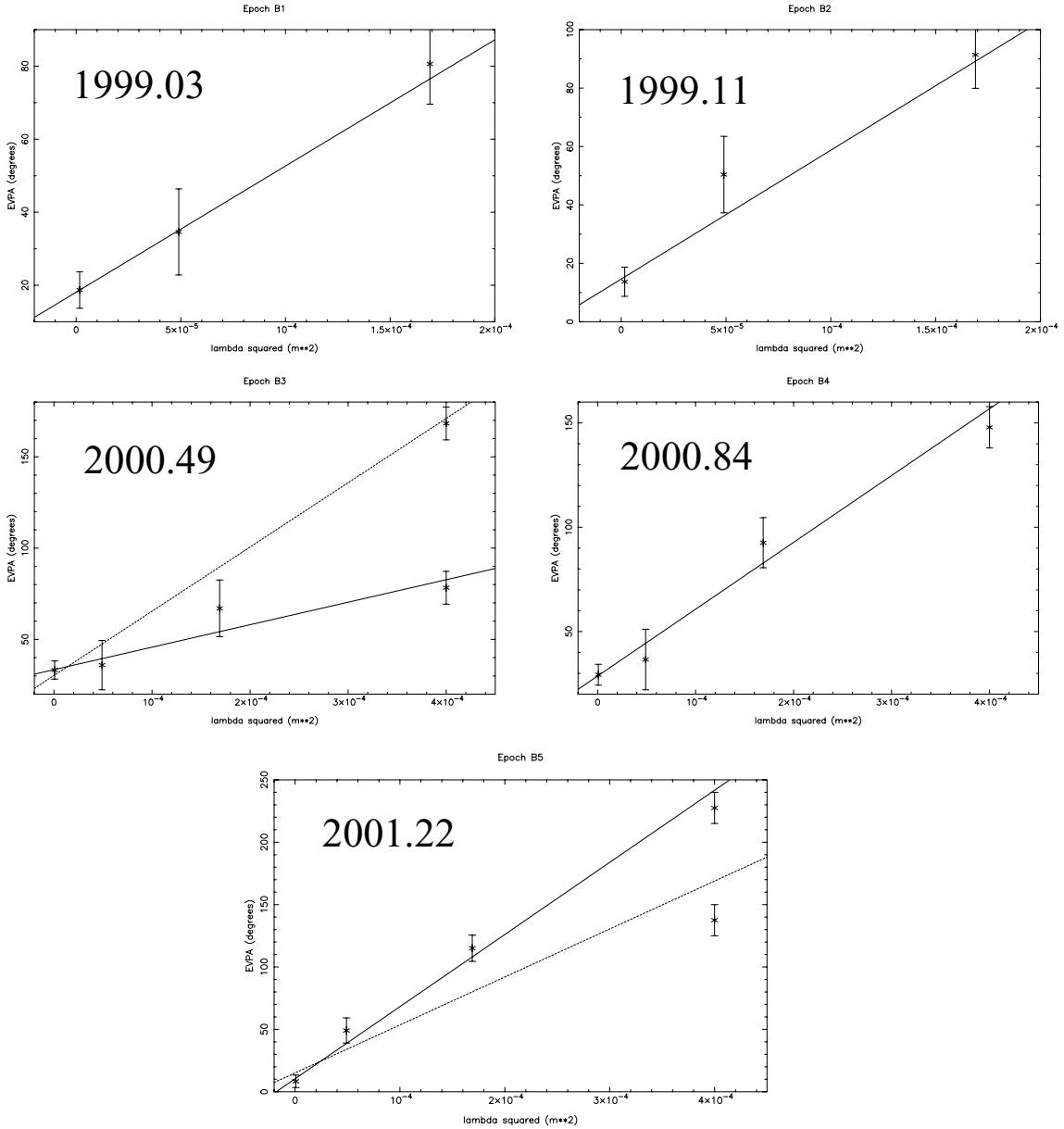

Figure 9. Plots of EVPA against λ^2 for supplementary epochs B1–B5. The solid line shows the best fit to these data allowing for 180° ambiguities and for a 90° ambiguity in the longest observing wavelength (20 mm) at epochs B3 and B5. For epochs B3 and B5 the dotted line represents the best fit to these data without allowing for a 90° ambiguity in the longest observing wavelength (as explained in the text).

Table 8. Faraday rotation measurements from supplementary data B1–B5. An asterisk (i.e. B3*, B5*) shows that the best fit has included a 90° ambiguity at 20 mm (as discussed in the text).

Epoch	Rotation measure (rad m^{-2})	Intrinsic EVPA (deg)	Red. χ^2
B1	6032 ± 1173	18.1 ± 4.8	0.0001
B2	7702 ± 1202	14.6 ± 4.3	1.45
B3*	2151 ± 468	33.4 ± 4.7	0.36
B3	6142 ± 468	30.2 ± 4.7	2.03
B4	5590 ± 500	28.7 ± 4.7	0.28
B5*	$10\,091 \pm 576$	10.4 ± 4.5	0.74
B5	6710 ± 576	15.1 ± 4.5	8.1

Table 9. These data give a comparison for epochs B1–B5 of the observed EVPA (measured at 7 mm), the corrected EVPA (assuming a homogeneous external Faraday screen) and the SPA.

Epoch	Observed EVPA (deg)	Corrected EVPA (deg)	SPA (deg)
B1	34.6 ± 9.0	18.1 ± 4.8	7.7 ± 6.3
B2	50.4 ± 9.4	14.6 ± 4.3	7.8 ± 15.1
B3	35.9 ± 9.7	33.4 ± 4.7	18.9 ± 6.4
B4	36.6 ± 6.5	28.7 ± 4.7	21.5 ± 7.1
B5	49.1 ± 8.4	10.4 ± 4.5	21.9 ± 8.5

these regions in order to observe a $\propto\lambda^2$ dependence in the observed EVPAs. This would be the case for a straight jet with a transverse magnetic field. The observed departures from ΔEVPA $\propto \lambda^2$ at 20 mm in epochs B3 and B5 may then represent a gradient in RM (in the external medium) with distance from the central engine rather than self-absorption. This suggestion is consistent with the much lower RM measured on the spatial scales of lower-frequency VLBI observations (Reynolds et al. 2001).

5 TRAJECTORIES IN THE EXTENDED RADIO JET

The trajectories of components in the extended jet of BL Lac are variable. Mutel et al. (1990) found evidence of components travelling rectilinearly and components showing significant bending to the east after 1–2 mas travel from the core. The analysis of component trajectories performed by Denn et al. (2000) and Tateyama et al. (1998) for BL Lac utilized the plasma instability model of Hardee (1987), representing helical motions on the surface of a steady cone. Tateyama et al. (1998) preferred adiabatic to isothermal expansion and derived values of 17° for the angle of the cone axis to the line of sight and 2°.6 for the half cone angle. Denn et al. (2000) found $9^\circ \pm 2^\circ$ and $2^\circ.1 \pm 0^\circ.4$ for these angles and also preferred adiabatic to isothermal expansion. These adiabatic models predict highly curved trajectories near to the core as the wavelength of the helix increases with the distance from the cone apex. Tateyama et al. (1998) used their derived helical pitch angle to fit the components S1 and S3 from Mutel et al. (1990), and hence suggested that the initial pitch angle is the same from one component to the other. Denn et al. (2000) analysed four components (including C2 from Tateyama et al. 1998) and found that very different pitch angles were required. They concluded that the helical structure is unstable

Table 10. Properties of evolving components as detected at 7 mm. The x and y positions are relative to core component C1. We give the positional errors derived from the Brandeis software, these are combined with an error of 0.1 of the average beamsize (0.26×0.17 mas^2) in the subsequent trajectory fitting. I, P, χ and FWHM are the total and polarized flux densities, the EVPA and the component size, respectively.

Epoch	Comp. ID	x (mas)	y (mas)	I (mJy)	P (mJy)	χ (deg)	FWHM (mas)
1997.58	S10	-0.31 ± 0.01	-0.88 ± 0.01	140 ± 31	–	–	0.31 ± 0.04
1998.23	S10	-0.38 ± 0.01	-1.72 ± 0.01	887 ± 178	130 ± 30	-21 ± 10	0.37 ± 0.01
1998.41	S10	-0.55 ± 0.01	-1.89 ± 0.01	591 ± 127	88 ± 19	3 ± 9	0.53 ± 0.01
1998.58	S10	-0.52 ± 0.01	-1.96 ± 0.01	383 ± 77	32 ± 7	18.6 ± 9	0.59 ± 0.02
1998.58	S11	-0.23 ± 0.03	-0.55 ± 0.04	33 ± 12	–	–	0.08 ± 0.15
1998.76	S10	-0.52 ± 0.02	-2.02 ± 0.01	280 ± 57	15 ± 9	28 ± 20	0.60 ± 0.02
1998.76	S11	-0.36 ± 0.02	-0.76 ± 0.02	22 ± 12	–	–	0.05 ± 0.10
1998.94	S10	-0.71 ± 0.01	-2.28 ± 0.01	207 ± 42	51 ± 12	7 ± 8	0.47 ± 0.02
1998.94	S11	-0.57 ± 0.02	-1.05 ± 0.02	31 ± 9.3	–	–	0.18 ± 0.09
1999.03	S11	-0.50 ± 0.03	-0.99 ± 0.04	87 ± 24	–	–	0.14 ± 0.05
1999.11	S10	-0.61 ± 0.01	-2.46 ± 0.02	154 ± 44	–	–	0.41 ± 0.03
1999.12	S10	-0.75 ± 0.01	-2.35 ± 0.01	213 ± 46	69 ± 14	-4 ± 10	0.55 ± 0.01
1999.12	S11	-0.65 ± 0.02	-1.30 ± 0.04	30 ± 7	–	–	0.12 ± 0.05
1999.32	S10	-0.39 ± 0.03	-2.55 ± 0.02	195 ± 45	71 ± 10	1 ± 10	0.74 ± 0.07
1999.32	S11	-0.58 ± 0.04	-1.56 ± 0.03	71 ± 28	–	–	0.31 ± 0.05
1999.32	S12	-0.34 ± 0.07	-0.68 ± 0.03	22 ± 11	5 ± 6	42 ± 15	0.18 ± 0.04
1999.55	S10	-0.14 ± 0.03	-2.71 ± 0.03	105 ± 24	32 ± 8	9 ± 9	0.54 ± 0.04
1999.55	S11	-0.75 ± 0.03	-1.73 ± 0.03	184 ± 47	–	–	0.57 ± 0.03
1999.55	S12	-0.44 ± 0.04	-1.04 ± 0.04	20 ± 9	–	–	0.24 ± 0.06
1999.55	S13	-0.29 ± 0.02	-0.57 ± 0.03	40 ± 9	–	–	0.11 ± 0.08
1999.76	S10	-0.02 ± 0.14	-3.04 ± 0.14	28 ± 7	–	–	0.43 ± 0.11
1999.76	S11	-0.83 ± 0.01	-2.17 ± 0.02	134 ± 33	–	–	0.47 ± 0.06
1999.76	S12	-0.63 ± 0.03	-1.50 ± 0.02	99 ± 21	35 ± 9	52 ± 14	0.37 ± 0.09
1999.76	S13	-0.46 ± 0.01	-0.91 ± 0.02	104 ± 21	–	–	0.34 ± 0.02
1999.93	S12	-0.75 ± 0.01	-1.74 ± 0.02	277 ± 70	35 ± 9	68 ± 9	0.65 ± 0.02
2000.07	S11	-0.49 ± 0.01	-2.69 ± 0.01	23 ± 19	–	–	0.04 ± 0.08
2000.07	S12	-0.81 ± 0.01	-2.14 ± 0.03	70 ± 43	17 ± 6	44 ± 11	0.24 ± 0.04
2000.07	S13	-0.70 ± 0.02	-1.62 ± 0.02	195 ± 40	–	–	0.54 ± 0.03
2000.26	S11	-0.68 ± 0.03	-2.98 ± 0.03	81 ± 18	–	–	0.62 ± 0.04
2000.26	S12	-0.94 ± 0.04	-2.43 ± 0.04	127 ± 26	–	–	0.59 ± 0.04
2000.26	S13	-0.76 ± 0.01	-1.82 ± 0.02	162 ± 34	67 ± 16	55 ± 8	0.40 ± 0.02
2000.49	S11	-0.53 ± 0.22	-3.21 ± 0.23	70 ± 37	–	–	1.05 ± 0.17
2000.49	S13	-0.93 ± 0.03	-2.25 ± 0.03	314 ± 79	60 ± 13	56 ± 11	0.53 ± 0.16
2000.54	S11	-0.58 ± 0.03	-3.18 ± 0.04	79 ± 18	–	–	0.79 ± 0.06
2000.54	S13	-0.95 ± 0.02	-2.33 ± 0.02	355 ± 71	54 ± 8	59 ± 10	0.48 ± 0.02
2000.75	S11	-0.64 ± 0.08	-3.43 ± 0.38	49 ± 89	–	–	1.14 ± 0.97
2000.75	S13	-0.99 ± 0.01	-2.73 ± 0.01	340 ± 71	70 ± 9	54 ± 8	0.60 ± 0.02
2000.84	S11	-0.08 ± 0.58	-3.57 ± 1.09	20 ± 100	–	–	2.3 ± 1.34
2000.84	S13	-0.94 ± 0.01	-2.88 ± 0.01	279 ± 57	53 ± 49	57 ± 11	0.80 ± 0.02
2000.95	S13	-0.87 ± 0.01	-3.05 ± 0.03	228 ± 46	67 ± 15	47 ± 9	0.84 ± 0.04
2001.22	S13	-0.93 ± 0.12	-3.55 ± 0.05	96 ± 63	–	–	1.2 ± 0.11
2001.28	S13	-0.84 ± 0.04	-3.91 ± 0.04	91 ± 18.8	21 ± 8	50 ± 10	1.17 ± 0.08

between components. Clearly, the helical trajectories interpretation has problems that may be further investigated by the measurement of component evolution close to the core. This requires observations at the highest angular resolutions available. In this section we discuss the evolution of model-fitted components in the extended jet.

5.1 Trajectories of identified components

All of the 7-mm data sets were model-fitted similarly to that shown in Fig. 3. We identified four components with an approximately constant change in radial separation from the core with time. The first of these was recognized as being a continuation of component S10 described in Denn et al. (2000). We continue this naming scheme and denote these four components of S10–S13. The positions, total and polarized flux densities and sizes of these components are given in Table 10. The trajectories of each component are shown in Fig. 10. In earlier images, which were generally taken at much lower frequencies, the extended structure is dominated by one or two bright superluminal components (Tateyama et al. 1998). In several of the images presented in this paper we see a narrow and rather featureless jet in total intensity, e.g. epochs 1999.32 and 2000.26. However, with the exception of S11, these components were easily detected and well defined in the linear polarization model fits. The polarized components were generally found to have an EVPA approximately parallel to the component motion. S11 may then represent a bright region of quiescent jet rather than a travelling shock front. A faint component with a constant radial separation from the core of $\sim$1.5 mas was detected in the final five epochs of Fig. 1. This static component may be a permanent feature that is confused with moving features or beneath the noise level in some images.

The component trajectories vary between rectilinear (S12) and very bent (S10), with any deviation from rectilinearity being to the east. The sharp bend in the trajectory of S10 is in poor agreement with that predicted by the helical model (shown in fig. 23 of Denn et al. 2000); although only part of a larger component may have been fitted as a result of overresolving S10 at 7 mm. All components increase in size as they evolve and initially in flux density also. This is illustrated in Fig. 11, where the evolution in size and flux density of the highly polarized component S13 (maximum m of 41 per cent) is plotted. The maximum flux density of component S13 occurs near to the point where it deviates from rectilinear motion. This is not the case for S10–S12. The 7-mm and 1.3-cm model fits from epochs 2000.49 and 2000.84 give spectral indices, α, for S13 of -0.49 and -0.66, respectively (with $S_\nu \propto \nu^{+\alpha}$), suggesting that the component also becomes optically thin around the time of peak flux density.

5.2 Comparison with the predicted ejection position angle

In this section we investigate whether the trajectories of evolving components are compatible with the oscillation of the base of the jet. In order to derive the ejection position angles and ejection dates of the components shown in Fig. 10 we performed least-squares fitting to the positions and radial separations of each component. This was performed using only data points from the inner jet, before significant bending or deceleration was apparent. The least-squares fits to the positions and radial motions for component S13 are shown in Fig. 12. This process was also performed for the components S7–S10 using data adopted from Denn et al. (2000) (table 3 and figs 20–23) and Tateyama et al. (1998). We include the 1995.42 data point from fig. 21 of Denn et al. (2000), giving a higher apparent speed for S8 than quoted in that paper. Our 7-mm data were not included in the fitting for S10, owing to unknown frequency-dependent positional shifts in the origin. The results are given in Table 11. We find that only the fit to component S13 is inconsistent with having passed through the origin. This is probably the result of a slightly bent trajectory. The time taken to travel the distance between the origin

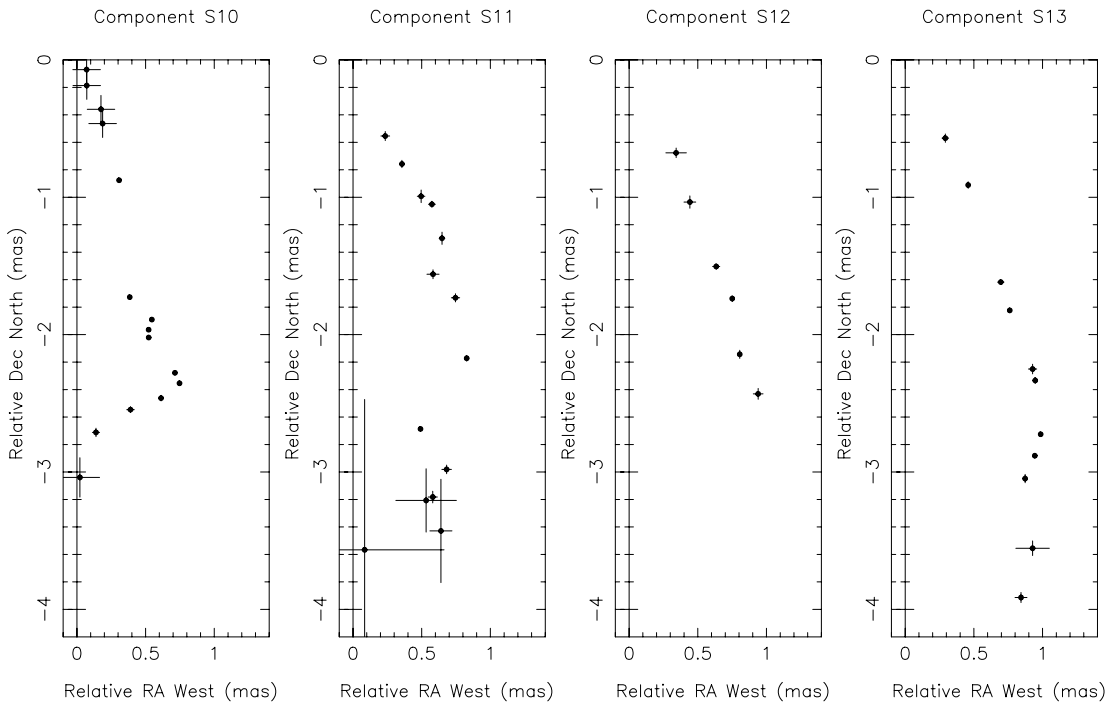

Figure 10. Trajectories of the components tabulated in Table 10. The error bars show approximate 1σ errors in the derived positions.

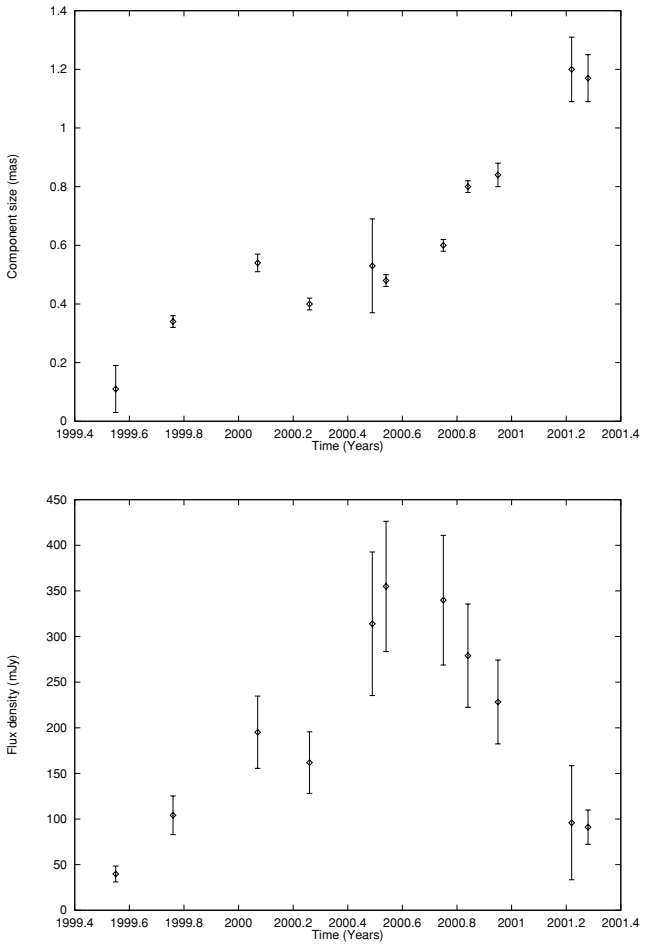

Figure 11. The top plot shows the variation in size of component S13 with time. The bottom plot shows the variation in flux density of component S13 with time.

and the intercept with the right ascension axis is included as a further contribution to the derived error in the ejection date.

The position angles of these components should be in agreement at the derived ejection dates with those predicted by the observed core oscillations (described in Section 4.1) if the inner jet trajectories can be described by approximately rectilinear motion at a constant apparent speed. The values derived for components S7–S13 are compared with the ejection position angle in Fig. 13. The agreement is reasonable for all seven components. However, as noted by Tateyama et al. (1998), there is a trend for components to be ejected at constant position angles of $\sim 190^\circ$ and $\sim 200^\circ$. Fig. 13 demonstrates that this does not necessarily require a sudden jump in ejection position angle from one component to another. Further monitoring is underway to investigate whether the majority of components are ejected to the western side of the mean nozzle position angle.

5.3 A ballistic model for the inner jet of BL Lac

In order to further investigate whether a ballistic model was appropriate for the inner jet of BL Lac we applied the kinematic model developed for the galactic X-ray binary SS 433 (Hjellming & Johnston 1981; Stirling et al. 2002) to the model-fitted components derived from the 23 epochs of 7-mm observations. The kinematic model uses the four parameters derived in Section 4.1, namely the phase-zero time, semi-amplitude, period and mean position angle on the sky plane. The final three parameters in the kinematic model were distance, velocity and inclination angle of the precession cone axis. Distance was derived from the redshift, using the luminosity distance, $D_{\rm L}$, for $h = 0.75$ to calculate the angular size distance$=D_{\rm L}/(1 + z)^2$ [note that the derived proper motions were also increased by $(1 + z)$ to allow for time dilation between source and observer frames]. Unfortunately, the jets of BL Lac appear one-sided, unlike in SS 433, which means that the origin of the kinematic model is undefined. We chose the location of C1 as our origin. Recent work on another nearby galaxy (3C 120) suggests that, at 7 mm, the radio core is within 0.2 mas of the accretion environment when projected on to the plane of the sky (Marscher et al. 2002).

For a precessing jet inclined to the line of sight the observed amplitude of oscillation is magnified as a result of projection effects by a factor of $1/\sin i$ (where i is the inclination angle to the axis of the precession cone). Estimates of the inclination angle for a non-precessing jet in BL Lac range from 40° (Hughes et al. 1989) to 9° (Denn et al. 2000), which would yield values for the intrinsic semi-amplitude of oscillation lower than that observed by factors of 0.63 and 0.17, respectively. The velocity and the inclination angle of each epoch were solved for using a χ^2 minimization over a 100×100 grid. The grid search in velocity and inclination angle corresponds to ranges of 0.9009–$0.9999c$ and 1°–$40\overset{\circ}{.}6$, respectively. An error equivalent to a tenth of the convolving beam was combined with the positional errors to prevent components with erroneously small errors dominating the final fits. The fitting procedure was performed for a nozzle precessing in both senses ($s = 1$ and -1, e.g. Stirling et al. 2002). The phase-zero point corresponds to the approaching jet being at its furthest point from the line of sight, which could be either of the points where the SPA equals the mean angle on the sky plane (in a single period) as shown in Fig. 4. For $s = 1$ and -1 phase-zero points of 1998.21 and 1999.17, respectively, were used. The half-period rotation preserves the correct oscillatory behaviour on the plane of the sky.

The results from applying this simple model were variable, with reduced χ^2 values in the range 3.2 (epoch B5) to 26.8 (epoch 6) for the entire core-jet structures. The sense of the precessional motion was not well constrained as both $s = 1$ and -1 gave average reduced χ^2 values of 12 for all 23 epochs. Rectilinear motion over several periods would be necessary to constrain s as the light travel time between the front and back of the precession cone becomes more important with distance from the core.

Averaging the fits to β and i over the two senses of precession and over all epochs gave values of $\beta = 0.989c \pm 0.008c$ and $i = 9\overset{\circ}{.}2 \pm 5\overset{\circ}{.}5$. The fitted parameters will clearly be influenced by the curvature of trajectories shown in Fig. 10. However, we found that, in general, the averaged values for β and i gave a reasonable fit to the entire core structure ($\leqslant 1$ mas from the core) and not just the northerly components C1 and C2. Only three of the 23 epochs had a reduced $\chi^2 > 20$ for these core structures. A selection of the fits to the core structures, covering the entire time range of our observations and in approximate half-period spacings, are shown in Fig. 14. The agreement of the kinematic model to the observed core structure is very interesting given the assumptions of a constant outflow velocity, rectilinear motion for component evolution and the unknown position of the central engine. Fig. 14 also shows the worst fit of the model to the core structure (epoch 1999.93). It is not clear whether a varying ejection velocity or jitter in the ejection direction is responsible for the deviation from the model in this case.

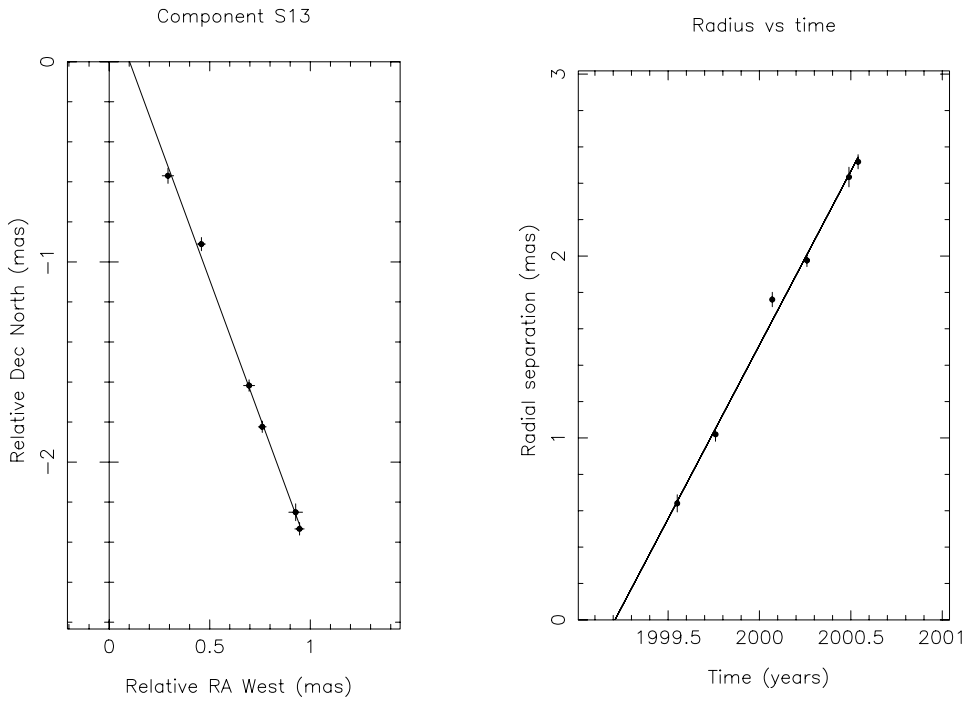

Figure 12. The plot on the left shows the variation in position of component S13 with time. The plot on the right shows the core to component radial separation with time.

Table 11. The ejection position angles, ejection dates and apparent speeds for the evolution of components S7–S13 close to the core. Epochs refers to the number of points used in each fit. Core error refers to how far the fitted line is from the origin in terms of the error in the intercept with the right ascension axis.

Comp. ID	Ejection date (yr)	Ejection PA (deg)	Proper motion (mas yr^{-1})	$\beta_{\rm app}$ ($h = 0.75$)	Epochs	Core error (σ)
S7	1994.27 ± 0.26	202.6 ± 4.6	1.4 ± 0.3	6.0 ± 1.2	8	1.0
S8	1995.17 ± 0.18	190.3 ± 3.1	1.8 ± 0.5	7.3 ± 1.9	5	2.4
S9	1996.40 ± 0.22	204.8 ± 5.5	1.9 ± 0.8	8.0 ± 3.5	5	0.1
S10	1996.63 ± 0.16	201.0 ± 4.5	0.7 ± 0.2	2.9 ± 0.9	4	0.7
S11	1998.17 ± 0.06	201.1 ± 2.8	1.4 ± 0.1	6.0 ± 0.3	8	0.8
S12	1998.94 ± 0.12	201.3 ± 1.4	1.9 ± 0.3	8.0 ± 1.1	4	1.4
S13	1999.21 ± 0.07	200.1 ± 0.5	1.9 ± 0.1	7.9 ± 0.4	6	5.2

6 DISCUSSION

6.1 Interpretation of an oscillating VLBI core

In the case of a binary orbiting black hole system, the rotation axis undergoes precession (e.g. Begelman, Blandford & Rees 1980). However, the period derived in this paper, $\sim$2 yr, is too short to be explained as a precession of a body of mass $\sim 10^8$ $M_\odot$. The Lense–Thirring effect may align the rotational axis of the central black hole with an accretion environment (Bardeen & Petterson 1975). This would be expected in a post-merger elliptical galaxy. For a maximally rotating black hole of 10^8 $M_\odot$ a Lense–Thirring precession period of the order of years is obtainable for an accretion radius of 10–100 Schwarzschild radii (Scheuer 1992). Any precession of the axis should be steady over time-scales of the order of years.

SS 433 shows evidence for precessing and nodding jets in the Doppler shifted lines and extended radio emission (e.g. Hjellming & Johnston 1981; Margon & Anderson 1989). Optical photometry demonstrates that the accretion disc is also precessing and nodding. It seems probable that the accretion disc in SS 433 can impose its orientation on the mildly relativistic jets (e.g. Vermeulen 1989). SS 433 has shown no detectable change in precessional period over 20 years of monitoring but exhibits substantial noise-like residuals from an ideal periodic precession (Eikenberry et al. 2001).

The BL Lac object OJ 287 has been reported to exhibit periodicities of 12 and 1.67 yr with the longer period probably connected with an eclipse owing to orbital motion of the central binary black hole system (e.g. Valtonen, Lehto & Pietilä 1999). This periodicity was alternatively interpreted as a torque exerted by a companion mass on the accretion disc, similar to that postulated for SS 433 and Hercules X-1 (Katz 1997). Fan et al. (2002) reports period detections (from 1 to 18 yr) in the optical light curves of nine separate BL Lac objects. If these inferences are correct, then periodicities must be common in BL Lac objects. This could be explained by the Lense–Thirring effect or by the torque provided by a companion black hole.

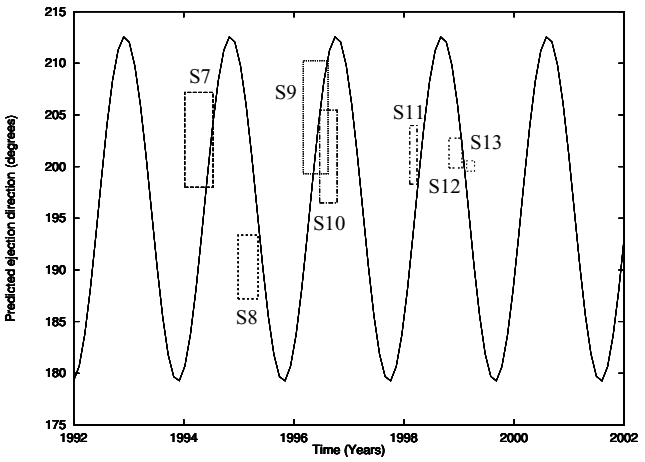

Figure 13. The sinusoidal oscillation of the core of BL Lacertae as derived from our 7- and 1-mm data. The error boxes give 1σ errors on the ejection date and position angle of recently ejected components in the jet.

6.2 Non-detection of a counter jet

Earlier we suggested that the core components, denoted by C1 and C2, represented the transition regime from an optically thick to an optically thin jet. However, it is possible that in C1 we are detecting a weaker counter-jet. Apparent speeds greater than $5c$ are typically observed (Tateyama et al. 1998; Denn et al. 2000), giving an upper limit for the inclination, i, of $\sim 23^\circ$ and a lower limit for the velocity (in terms of c), β, of ~ 0.98. We can approximate the ratio of the flux densities for the approaching and receding jets, $S_{\rm app}/S_{\rm rec}$, as $[(1+\beta\cos i)/(1-\beta\cos i)]^{2-\alpha}$ (e.g. Mirabel & Rodriguez 1994). Using the mean spectral index between 7 and 13 mm for C1 of $\alpha = 0.8$ (for C2 the mean $\alpha = -0.36$) this ratio is minimized for $\beta = 0.98$ and $i = 23$, with a value of ~ 35. The flux density of the receding jet should therefore be a very small fraction of the total flux density measurement. At epoch 2000.26 the component C1 was observed to contribute more than 25 per cent of the total flux density of the source, as measured by a single dish at 8 mm (H. Teräsranta, private communication). It therefore seems very unlikely that C1 represents a counter jet.

6.3 A precessing nozzle

We assume then that components C1 and C2 represent the base of the approaching radio jet (as seen at 7 mm), which is oscillating on the plane of the sky owing to the precession of the central engine. Inspection of the trajectories and apparent speeds of components S7–S10 from Denn et al. (2000), S1 and S2 from Reynolds (2002) and analysis of the model-fitted components in these 7-mm VLBA observations suggest that a rectilinear model for component evolution is a reasonable assumption on angular scales less than 1–2 mas from the core. The observed radio jet structure on deca-parsec scales is not consistent with a simple precessing nozzle as it curves to the southeast, at a position angle outside the range we observe for the 7-mm SPA. This is perhaps the consequence of a cross-wind in the interstellar medium (Lim & Steffen 2001), or a larger-scale helical trajectory. Alternatively, it might be explained by associating our observed SPA oscillation with the nodding motion of a longer period of precession.

A precessing base to the radio jet will give a varying component in any flux density measurements simply caused by the changing angle to the line of sight. We can estimate the magnitude of this variation using the values of $i = 9\overset{\circ}{.}4$ and $\beta = 0.989$ derived from the kinematic model fitting. We use the measured semi-amplitude of oscillation (projected on to the sky) of $16\overset{\circ}{.}7$, giving a deprojected semi-amplitude, θ, of $16\overset{\circ}{.}7 \times \sin i$. We also assume an unvarying pattern emitting isotropically in its rest frame. We assume the observed flux density is proportional to $D^{2-\alpha}$, where D is the Doppler factor. The ratio of the maximum to the minimum observed flux density, $S_{\rm r} = S(i-\theta)/S(i+\theta)$, from this pattern (for $\alpha = 0$) is 3.4. The JCMT light curve in Fig. 2 shows that flaring events observed over the period of monitoring are of large amplitude (four to five times the quiescent level) and variable time-scale, making a period detection problematic. This is illustrated by plotting the minimized χ^2 of a sine wave fit to these JCMT data after detrending and folding at each trial frequency, shown in Fig. 15. The lack of a clear detection at frequencies near 0.5 $\rm yr^{-1}$ argues against a large inclination angle as the periodic total intensity variations would dominate the flaring variations in this case ($i = 40^\circ$ gives $S_{\rm r} = 7.4$). Lower-frequency flux-density monitoring may well be contaminated by the evolution of bright components on more extended size scales.

6.4 Variable Faraday rotation in an external screen

In Section 4.2 we derived Faraday rotation measures for the component C2 of 2000–10 000 rad $\rm m^{-2}$ (corresponding to EVPA rotations of 6°–30° at 7 mm). The linear relationship between RM and λ^2 suggests that this is caused by an external screen of magnetized plasma. It is not clear from Table 7 whether frequency-dependent depolarization was also present. Component C1 was generally unpolarized except for epoch 1998.58 with $m = 4.7$ per cent and a 70° misalignment from a transverse field. The EVPA offset from its intrinsic value (in radians) is $\Delta{\rm EVPA} = {\rm RM}\lambda^2$, where λ is in metres. For a homogeneous foreground slab of plasma the RM is equal to the Faraday depth; therefore, ${\rm RM} = 8.1 \times 10^3 (1+z)^2 \int_0^d n_{\rm e} B_{||}\, {\rm d}s$, with $B_{||}$ in tesla, $n_{\rm e}$ is the thermal electron density in $\rm m^{-3}$ and d is the path-length of the slab in pc. The column density of electrons required to produce an observed RM of 10 000 rad $\rm m^{-2}$ is $4.3 \times 10^{25}/B_{||}$ $\rm m^{-2}$, with $B_{||}$ in nT. We also observe a relatively smooth variation in RM with time (see Fig. 5), assuming that the (EVPA−SPA) offsets are a result of a Faraday screen. This indicates that the screen is not excessively clumped, or if it is then the covering factor is low.

Although we did not identify a periodicity in the 7-mm (EVPA−SPA) data (Fig. 5) the good straight line fits between EVPA and λ^2 shown in Fig. 9 strongly imply that at these epochs, the derotated 7-mm EVPAs are equal to the 1-mm EVPAs measured at the JCMT. The good correlation between the 1-mm EVPA and 7-mm SPA (Section 4.1) then implies that, at the epochs of the supplementary data, the 7-mm EVPAs are also equal to the SPA at the 7-mm core, as expected in a jet with a transverse magnetic field. It is possible that the 7-mm (EVPA−SPA) offset and therefore the core RM are both periodic phenomena, and that our failure to detect a period in the (EVPA−SPA) data is owing to the limited sampling, large uncertainties and perhaps a number of 'outlier' points. Such a periodicity could be the result of a periodically varying path-length to the core through an external Faraday screen such as the ionized gas in the nuclear region (Taylor 2000) or a cocoon surrounding the jet itself (Aloy et al. 1999). The difficulties of analysing the broad line region using RM measurements of sources at different distances

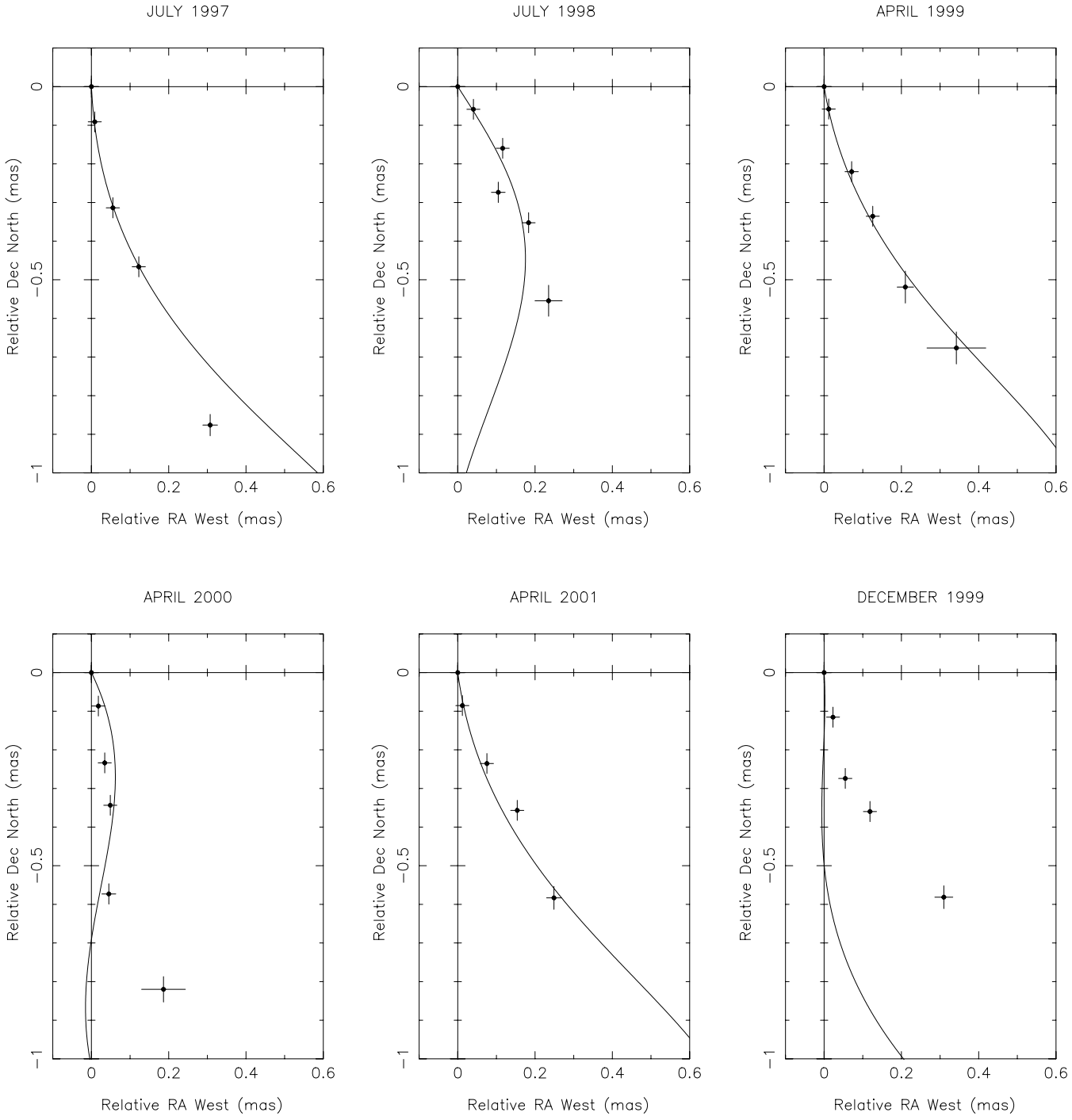

Figure 14. The solid lines are the predicted ridgelines of a ballistic jet using the four parameters derived in Section 4.1, $\beta = 0.989c$, $i = 9.^{\circ}2$ and $s = -1$. The top row (from left to right) shows the model fits of the core structure for epochs B0 (reduced $\chi^2 = 6.0$), 3 (2.2) and 7 (0.2), the bottom row shows 12 (8.4), 17 (1.2) and 10 (67.6). Epoch 10 is included to demonstrate the largest observed deviations from the kinematic model.

and inclination angles is discussed in Reynolds et al. (2001). It is clear that a more regular set of observations at wavelengths between 1 mm and 2 cm is required to investigate the time dependence of the RM and to make inferences concerning the distribution of gas that constitutes the Faraday screen. Direct inferences concerning the motion of the jet axis parallel to the line of sight must also await such observations.

6.5 Complex extended jet evolution

Previous work (Tateyama et al. 1998; Denn et al. 2000) on the evolution of components in the jet has shown assumed helical trajectories that increase in curvature towards the core. This interpretation requires that the jet structure near the core is oriented randomly with time (in order to agree with previous observations). Our

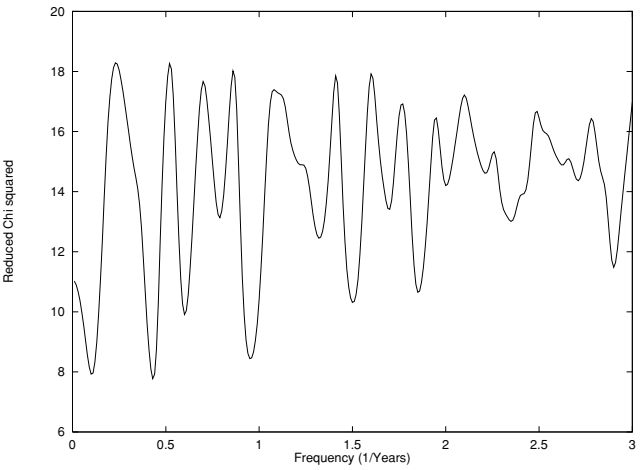

Figure 15. At each trial period the detrended total intensity JCMT data (shown in Fig. 2) were folded, then fitted with a sine curve. Reduced χ^2 values are plotted as a function of trial frequency and the minima in the plot suggest the most probable periods.

observations suggest relatively straight trajectories near the core, increasing in curvature at large distances (greater than 1–2 mas) from the core ejected in a direction that (at least during our observing period) varied sinusoidally (and not randomly) with time. Furthermore, the observed continuation of the trajectory of component S10 (reported earlier by Denn et al. 2000) did not fit Denn's prediction from the helical trajectory model.

Such a precessing engine can drive wave–wave interactions in a jet giving standing and moving features in the extended jet (Hardee et al. 2001). Simulations of a $\gamma = 5$ jet precessing with an $11\overset{\circ}{.}25$ opening semi-angle show that the flow is approximately ballistic, with velocity vectors not aligned with the local jet direction (Hughes, Miller & Duncan 2002). The extent to which a propagating shocked fluid, thought to explain moving VLBI components, will follow the helical channel or follow approximately ballistic trajectories is a subject for future numerical study. Recent unpublished simulations of precessing jets show that shocks can initially behave in a ballistic fashion, undergoing a transition to a non-ballistic flow once they have expanded sufficiently (Gómez, private communication). These numerical results are consistent with the initially straight component trajectories and the subsequent bending and expansion of the jet in BL Lac.

7 CONCLUSIONS

Four lines of evidence are presented in support of the hypothesis that the direction of ejection of plasma at the base of the jet in BL Lac varies sinusoidally with time in a manner consistent with ejection from a precessing nozzle.

First, over four years of VLBA monitoring at 7 mm we detected a sinusoidal oscillation in the base of the radio jet. The period of oscillation was 2.29 ± 0.35 yr, and the semi-amplitude was $12\overset{\circ}{.}2 \pm 7\overset{\circ}{.}8$ (projected on to the sky) about a mean position angle of $191\overset{\circ}{.}2 \pm 5\overset{\circ}{.}5$. Since the jet is known to display superluminal motion, it seems highly probable that this oscillation is the manifestation of a much smaller oscillation in the jet direction that has been amplified by projection.

Secondly, 1-mm JCMT monitoring over the same period (but with some archival data over a period of 10 years) revealed a similar oscillation in EVPA with amplitude, phase, period and offset all in good agreement with those of the 7-mm structural position angle. Over a more limited period of 1 yr, the optical EVPAs were also in good agreement with the 7-mm SPA. Since the polarization in BL Lac objects is known to be largely parallel to the jet direction, this result implies that the jet direction is the same on scales responsible for 1-mm emission as on larger scales responsible for 7-mm emission.

Thirdly, using our data and that of Tateyama et al. (1998) and Denn et al. (2000) we have been able to identify ejection dates and trajectories for a total of seven components. The trajectories are nearly straight over the first few mas, and the derived directions are consistent with the core orientations at the ejection date derived from the 7-mm core and JCMT data.

Finally, at most of the epochs, the observed structures (as characterized by all the model components, not just those that can be traced between epochs) matched those predicted by a constant-speed precessing jet with parameters $\beta = 0.989c \pm 0.008c$ (for $h = 0.75$) and $i = 9\overset{\circ}{.}2 \pm 5\overset{\circ}{.}5$ (giving an intrinsic oscillation semi-amplitude of $2\overset{\circ}{.}7$ as compared with the observed amplitude of $16\overset{\circ}{.}7$ derived by fitting the 7- and 1-mm data). Deviations at some epochs may be as a result of departures from our assumption of absolutely constant speed and completely straight trajectories.

We conclude that over the first 1–2 mas, the jet in BL Lac is well characterized by a constant speed precessing jet. The results are far more consistent with this model than the earlier helical-trajectory models; these predicted increasing curvature towards the core and this is not observed. On angular scales greater than 2 mas from the core a transition to non-ballistic fluid motion occurs. Further monitoring to confirm these observed oscillations in 7-mm structural position angle and 1.3-/0.85-mm EVPA would seem essential. If further measurements of the period are consistent with these results then that would strengthen the case that the oscillation represents precession in a binary black hole system. Any future departure from consistency with the periodicity derived from our measurements would suggest that the apparent periodicity is not a stable phenomenon. In this case, we would need to explain the quasi-cyclic behaviour in terms of hydrodynamic or magnetic instabilities rather than precession of the accretion disc round the black hole.

ACKNOWLEDGMENTS

TVC and AMS acknowledge support from PPARC. The VLBA is an instrument of the National Radio Astronomy Observatory, which is a facility of the National Science Foundation operated under cooperative agreement by Associated Universities, Inc. We thank Harri Teräsranta of the Metsahovi Observatory for providing single-dish flux densities at 22 and 37 GHz. The JCMT is operated by the Joint Astronomy Centre in Hilo, Hawaii on behalf of the parent organizations Particle Physics and Astronomy Research Council in the United Kingdom, the National Research Council of Canada and The Netherlands Organization for Scientific Research. The Boston University contribution was supported in part by the US National Science Foundation through grants AST9802941 and AST0098579.

REFERENCES

Aloy M.A., Ibáñez J.M., Martí J.M., Gómez J.L., Müller E., 1999, ApJ, 523, 125
Bardeen J.M., Petterson J.A., 1975, ApJ, 195, L62
Begelman M.C., Blandford R.D., Rees M.J., 1980, Nat, 287, 307
Brindle C. et al., 1985, MNRAS, 214, 619
Burn B.J., 1966, MNRAS, 133, 67

Corbett E.A., Robinson A., Axon D.J., Hough J.H., Jeffries R.D., Thurston M.R., Young S., 1996, MNRAS, 281, 737
Denn G.R., Mutel R.L., Marscher A.P., 2000, ApJS, 129, 61
Eikenberry S.S., Cameron P.B., Fierce B.W., Kull D.M., Dror D.H., Houck J.R., Margon B., 2001, ApJ, 561, 1027
Fan J.H., Lin R.G., Xie G.Z., Zhang L., Mei D.C., Su C.Y., Peng Z.M., 2002, A&A, 381, 1
Fomalont E., 1981, News. NRAO, 3, 3
Gabuzda D.C., Cawthorne T.V., 2000, MNRAS, 319, 1056
Greaves J.S. et al., 2003, MNRAS, in press
Hagen-Thorn V.A., Marchenko S.G., Yakovleva V.A., 1985, Astrofiz., 22, 1
Hardee P.E., 1987, ApJ, 318, 78
Hardee P.E., Hughes P.A., Rosen A., Gomez E.A., 2001, ApJ, 555, 744
Hjellming R., Johnston K., 1981, Nat, 290, 100
Holland W.S. et al., 1999, MNRAS, 303, 659
Horne J.H., Baliunas S.L., 1986, ApJ, 302, 757
Hughes P.A., Aller H.D., Aller M.F., 1989, ApJ, 341, 68
Hughes P.A., Miller M.A., Duncan G.C., 2002, ApJ, 572, 713
Katz J.I., ApJ, 1997, 478, 527
Königl A., 1981, ApJ, 243, 700
Lim A.J., Steffen W., 2001, MNRAS, 322, 16
Lister M.L., 2001, ApJ, 562, 208
Leppanen K.J., Zensus J.A., Diamond P.J., 1995, AJ, 110, 2479
Margon B., Anderson S., 1989, ApJ, 347, 448
Marscher A.P. et al., 1999, Am. Astron. Soc., 195, 8902
Marscher A.P., Jorstad S.G., Gómez J.L., Aller M.F., Teräsranta H., Lister M.L., Stirling A.M., 2002, Nat, 417, 625
Mirabel I.F., Rodriguez L.F., 1994, Nat, 371, 46
Moore R.L. et al., 1982, ApJ, 260, 415
Moore R.L., Schmidt G.D., West S.C., 1987, ApJ, 314, 176
Mutel R.L., Denn G.R., 2000, Am. Astron. Soc., 197, 7508
Mutel R.L., Su B., Bucciferro R.R., Phillips R.B., 1990, ApJ, 352, 81
Nartallo R., Gear W.K., Murray A.G., Robson E.I., Hough J.H., 1998, MNRAS, 297, 667
Padovani P., 1992, MNRAS, 257, 404
Pearson T.J., Shepherd M.C., Taylor G.B., Myers S.T., 1994, American Astronomical Society Meeting, 185, 808
Reynolds C., 2002, PhD thesis, Univ. Central Lancashire
Reynolds C., Cawthorne T.V., Gabuzda D.C., 2001, MNRAS, 327, 1071
Roberts D.H., Gabuzda D.C., Wardle J.F.C., 1987, ApJ, 323, 536
Roberts D.H., Wardle J.F.C., Brown L.F., 1994, ApJ, 427, 718
Robson E.I., Stevens J.A., Jenness T., 2001, MNRAS, 327, 751
Scheuer P.A.G., 1992, Extragalactic Radio Sources. From Beams to Jets, 368
Schlegel D.J., Finkbeiner D.P., Davis M., 1998, ApJ, 500, 525
Smith P.S., Balonek T.J., Heckert P.A., Elston R., Schmidt G.D., 1985, AJ, 90, 1184
Stirling A.M., Jowett F.H., Spencer R.E., Paragi Z., Cawthorne T.V., Ogley R.N., 2002, MNRAS, 337, 657
Tateyama C.E., Kingham K.A., Kaufmann P., Piner B.G., De Lucena A.M.P., Botti L.C.L., 1998, ApJ, 500, 810
Taylor G.B., 1998, ApJ, 506, 637
Taylor G.B., 2000, ApJ, 533, 95
Valtonen M.J., Lehto H.J., Pietilä H., 1999, A&A, 342, L29
Vermeulen R.C., 1989, PhD thesis, Univ. Leiden
Vermeulen R.C., Ogle P.M., Tran H.D., Browne I.W.A., Cohen M.H., Readhead A.C.S., Taylor G.B., Goodridge R.W., 1995, ApJ, 452, L5
Wardle J.F.C., Kronberg P.P., 1974, ApJ, 194, 249

This paper has been typeset from a TEX/LATEX file prepared by the author.